

# Spin Dynamics in Hierarchical Black Hole Triples: Predicting Final Spin-Orbit Misalignment Angle From Initial Conditions

YUBO SU,<sup>1</sup> DONG LAI,<sup>1</sup> AND BIN LIU<sup>1</sup>

<sup>1</sup>*Cornell Center for Astrophysics and Planetary Science, Department of Astronomy, Cornell University, Ithaca, NY 14853, USA*

(Received XXXX; Revised XXXX; Accepted XXXX)

Submitted to ApJ

## ABSTRACT

Abstract

*Keywords:* keywords

### 1. INTRODUCTION

As the LIGO/VIRGO collaboration continues to detect mergers of black hole (BH) binaries (e.g. Abbott et al. 2016, 2019), it is increasingly important to systematically study various formation channels of BH binaries and their observable signatures. The canonical channel consists of isolated binary evolution, in which mass transfer and friction in the common envelope phase cause the binary orbit to shrink sufficiently that it subsequently merges via emission of gravitational waves (GW) within a Hubble time (e.g. Lipunov et al. 1997, 2017; Podsiadlowski et al. 2003; Belczynski et al. 2010, 2016; Dominik et al. 2012, 2013, 2015). BH binaries formed via isolated binary evolution are generally expected to have small misalignment between the BH spin axis and the orbital angular momentum axis (Postnov & Kuranov 2019; Belczynski et al. 2020). On the other hand, various flavors of dynamical formation channels of BH binaries have also been studied. These involve either strong gravitational scatterings in dense clusters (e.g. Zwart & McMillan 1999; O’leary et al. 2006; Miller & Lauburg 2009; Banerjee et al. 2010; Downing et al. 2010; Ziosi et al. 2014; Rodriguez et al. 2015; Samsing & Ramirez-Ruiz 2017; Samsing & D’Orazio 2018; Rodriguez et al. 2018; Gondán et al. 2018) or more gentle “tertiary-induced mergers” (e.g. Blaes et al. 2002; Miller & Hamilton 2002; Wen 2003; Antonini & Perets 2012; Antonini et al. 2017; Silsbee & Tremaine 2016; Liu & Lai 2017, 2018; Randall & Xianyu 2018; Hoang et al. 2018). The dynamical formation channels generally produce BH binaries with misaligned spins.

GW observations of binary inspirals can put constraints on BH masses and spins. Typically, spin constraints come in the form of two dimensionless mass-weighted combinations of the component BH spins: (i) the aligned spin parameter

$$\chi_{\text{eff}} \equiv \frac{m_1 \chi_1 \cos \theta_{s_1, l} + m_2 \chi_2 \cos \theta_{s_2, l}}{m_1 + m_2} \quad (1)$$

where  $m_{1,2}$  are the masses of the BHs,  $\theta_{s_i, l}$  is the angle between the  $i$ th spin and the binary orbital angular momentum axis, and  $\chi_i \equiv cS_i/(Gm_i^2)$  is the dimensionless Kerr spin parameter; and (ii) the perpendicular spin parameter (Schmidt et al. 2015)

$$\chi_p \equiv \max \left\{ \chi_1 \sin \theta_{s_1, l}, \frac{q(4q+3)}{4+3q} \chi_2 \sin \theta_{s_2, l} \right\}, \quad (2)$$

where  $q \equiv m_2/m_1$ . The systems detected in the O1 and O2 observing runs have small  $\chi_{\text{eff}}$ , which is consistent with either small  $\chi_1$  and  $\chi_2$  or highly misaligned BH spins ( $\theta_{s_i, l} \approx 90^\circ$ ). The recently-announced LIGO detection GW190521 (Abbott et al. 2020) has  $\chi_{\text{eff}} = 0.08^{+0.27}_{-0.38}$  while  $\chi_p = 0.68^{+0.25}_{-0.37}$ . The spin-orbit misalignment angles of the two merging BHs are reported to be  $81^{+64}_{-53}$  and  $85^{+57}_{-55}$  degrees respectively.

Liu & Lai (2017, 2018, hereafter LL17, LL18), and Liu et al. (2019) carried out a systematic study of binary BH mergers in the presence of a tertiary companion. LL17 pointed out the important effect of spin-orbit coupling (de-Sitter precession) in determining the final spin-orbit misalignment angles of BH binaries in triple systems. They considered binaries with sufficiently compact orbits (so that mergers are possible even without a tertiary) and showed that the combination of LK oscillations (induced by a modestly inclined tertiary) and spin-orbit coupling gives rise to a broad range of final spin-orbit misalignment in the merging binary BHs. We call these mergers *LK-enhanced mergers*. LL18 considered the most interesting case of *LK-induced mergers*, in which an

initially wide BH binary (too wide to merge in isolation) is pushed to extreme eccentricities (close to unity) by a highly inclined tertiary and merges within a few Gyrs. LL18 examined a wide range of orbital and spin evolution behaviors and found that LK-induced mergers can sometimes yield a “90° attractor”: when the BH spin is initially aligned with the inner binary angular momentum axis ( $\theta_{\text{sl},i} = 0$ ), it evolves towards a perpendicular state ( $\theta_{\text{sl},f} = 90^\circ$ ) near merger. Qualitatively, they found that the attractor exists when the LK-induced orbital decay is sufficiently “gentle” and the octupole effect is unimportant. Fig. 1 gives an example of a system evolving towards this attractor, where  $\theta_{\text{sl}}$  converges to  $\approx 90^\circ$  at late times in the bottom right panel. Fig. 2 shows how  $\theta_{\text{sl},f}$  varies when the initial inclination of the tertiary orbit  $I_i$  (relative to the inner orbit) is varied. Note that for rapid mergers (when  $I_i$  is close to  $90^\circ$ ), the attractor does not exist; as  $I_i$  deviates more from  $90^\circ$ , the merger time increases and  $\theta_{\text{sl},f}$  is close to  $90^\circ$ . This 90° attractor gives rise to a peak around  $\chi_{\text{eff}} = 0$  in the final  $\chi_{\text{eff}}$  distribution in tertiary-induced mergers (LL18; Liu et al. 2019). This peak was also found in the population studies of Antonini et al. (2018).

The physical origin of this 90° attractor and under what conditions it can be achieved are not well understood. LL18 proposed an explanation based on analogy with an adiabatic invariant in systems where the inner binary remains circular throughout the inspiral (LL17). However, this analogy is not justified, as significant eccentricity excitation is a necessary ingredient in LK-induced mergers. In addition, the LK-enhanced mergers considered in LL17 show no 90° attractor even though the orbital evolution is slow and regular.

In this paper, we study an analytic theory that reproduces the 90° attractor and characterizes its regime of validity. In Sections 2 and 3, we set up the relevant equations of motion for the orbital and spin evolution of the system. In Sections 4 and 5, we develop an analytic theory and compute its regime of validity for LK-induced mergers. In Section 6, we comment on the LK-enhanced scenario. We discuss and conclude in Section 8.

## 2. LK-INDUCED MERGERS: ORBITAL EVOLUTION

In this section we summarize the key features and relevant equations for LK-induced mergers to be used for our analysis in later sections. Consider a black hole (BH) binary with masses  $m_1$  and  $m_2$  having total mass  $m_{12}$ , reduced mass  $\mu = m_1 m_2 / m_{12}$ , semimajor axis  $a$  and eccentricity  $e$ . This inner binary orbits around a tertiary with mass  $m_3$ , semimajor axis  $a_{\text{out}}$  and eccentricity  $e_{\text{out}}$  in a hierarchical configuration ( $a_{\text{out}} \gg a$ ). Unless explicitly stated, we assume  $m_3 \gg m_1, m_2$  (so the tertiary is a supermassive black hole, or SMBH), although our analysis can be easily generalized to comparable masses. It is also convenient to define the effective outer

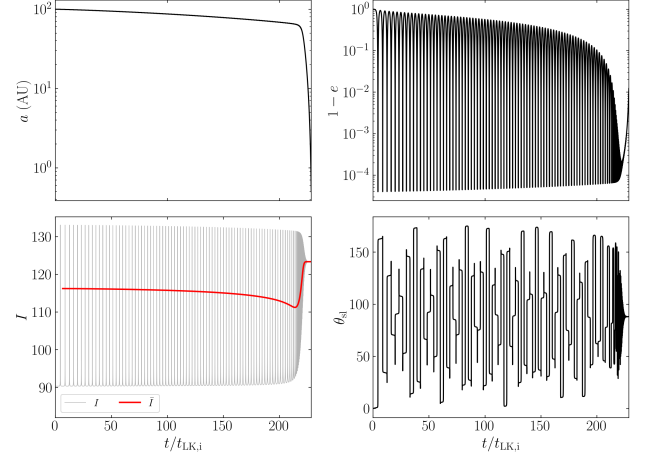


**Figure 1.** An example of the 90° spin attractor in LK-induced BH binary mergers. The four panes show the time evolution of the binary semi-major axis  $a$ , eccentricity  $e$ , inclination  $I$  [the red line denotes the averaged  $\bar{I}$  given by Eq. (29)], and spin-orbit misalignment angle  $\theta_{\text{sl}}$ . The unit of time  $t_{\text{LK},i}$  is the LK timescale [Eq. (10)] evaluated for the initial conditions. The inner binary has  $m_1 = 30M_\odot$ ,  $m_2 = 20M_\odot$ , and initial  $a_i = 100$  AU,  $e_i = 0.001$ ,  $I_i = 90.35^\circ$  (with respect to the outer binary), and  $\theta_{\text{sl},i} = 0$ . The tertiary SMBH has  $a_{\text{out}} = 2.2$  pc,  $e_{\text{out}} = 0$ , and  $m_3 = 3 \times 10^7 M_\odot$ . It can be seen that  $\theta_{\text{sl}}$  evolves to  $\sim 90^\circ$  as  $a$  shrinks to smaller values.

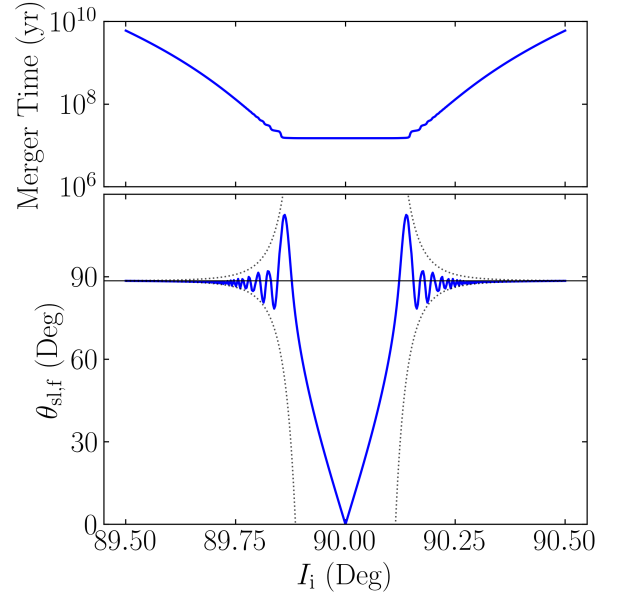


**Figure 2.** The merger time and the final spin-orbit misalignment angle  $\theta_{\text{sl},f}$  as a function of the initial inclination  $I_i$  for LK-induced mergers. The other parameters are the same as those in Fig. 1. For  $I_i$  somewhat far away from  $90^\circ$ , the resulting  $\theta_{\text{sl},f}$  are all quite near  $90^\circ$ . The horizontal black solid line shows the predicted  $\theta_{\text{sl},f}$  if  $\bar{\theta}_e$  is conserved, i.e. Eq. (57). The black dashed line in the lower panel shows Eq. (61), which provides an estimate for the deviation from the 90° attractor.

semimajor axis

$$\tilde{a}_{\text{out}} \equiv a_{\text{out}} \sqrt{1 - e_{\text{out}}^2}. \quad (3)$$

We denote the orbital angular momentum of the inner binary by  $\mathbf{L} \equiv L\hat{\mathbf{L}}$  and the angular momentum of the outer binary by  $\mathbf{L}_{\text{out}} \equiv L_{\text{out}}\hat{\mathbf{L}}_{\text{out}}$ . Since  $L_{\text{out}} \gg L$ , we take  $\mathbf{L}_{\text{out}}$  to be fixed.

The equations of motion governing the orbital elements  $a$ ,  $e$ ,  $\varnothing$ ,  $I$ ,  $\omega$  (where  $\varnothing$ ,  $I$ ,  $\omega$  are the longitude of the ascending node, inclination, and argument of periapsis respectively) of the inner binary are

$$\frac{da}{dt} = \left( \frac{da}{dt} \right)_{\text{GW}}, \quad (4)$$

$$\frac{de}{dt} = \frac{15}{8t_{\text{LK}}} e j(e) \sin 2\omega \sin^2 I + \left( \frac{de}{dt} \right)_{\text{GW}}, \quad (5)$$

$$\frac{d\varnothing}{dt} = \frac{3}{4t_{\text{LK}}} \frac{\cos I (5e^2 \cos^2 \omega - 4e^2 - 1)}{j(e)}, \quad (6)$$

$$\frac{dI}{dt} = -\frac{15}{16t_{\text{LK}}} \frac{e^2 \sin 2\omega \sin 2I}{j(e)}, \quad (7)$$

$$\frac{d\omega}{dt} = \frac{3}{4t_{\text{LK}}} \frac{2j^2(e) + 5 \sin^2 \omega (e^2 - \sin^2 I)}{j(e)} + \Omega_{\text{GR}}, \quad (8)$$

where we have defined

$$j(e) = \sqrt{1 - e^2}, \quad (9)$$

$$t_{\text{LK}}^{-1} \equiv n \left( \frac{m_3}{m_{12}} \right) \left( \frac{a}{\tilde{a}_{\text{out}}} \right)^3, \quad (10)$$

with  $n \equiv \sqrt{Gm_{12}/a^3}$  the mean motion of the inner binary. The GR-induced apsidal precession of the inner binary is given by

$$\Omega_{\text{GR}}(e) = \frac{3Gnm_{12}}{c^2 a j^2(e)}. \quad (11)$$

The dissipative terms due to gravitational radiation are

$$\left( \frac{da}{dt} \right)_{\text{GW}} = -\frac{a}{t_{\text{GW}}(e)}, \quad (12)$$

$$\left( \frac{de}{dt} \right)_{\text{GW}} = -\frac{304}{15} \frac{G^3 \mu m_{12}^2}{c^5 a^4} \frac{1}{j^{5/2}(e)} \left( 1 + \frac{121}{304} e^2 \right), \quad (13)$$

where

$$t_{\text{GW}}^{-1}(e) \equiv \frac{64}{5} \frac{G^3 \mu m_{12}^2}{c^5 a^4} \frac{1}{j^{7/2}(e)} \left( 1 + \frac{73}{24} e^2 + \frac{37}{96} e^4 \right). \quad (14)$$

Fig. 1 depicts an example of LK-induced mergers as calculated using the above equations. We adopt the following fiducial parameters: the inner binary has  $m_1 = 30M_{\odot}$ ,  $m_2 = 20M_{\odot}$ , initial  $a = 100$  AU,  $e_i = 0.001$ , and  $I_i = 90.35^\circ$ . We take the SMBH tertiary companion to have  $m_3 = 3 \times 10^7 M_{\odot}$  and  $\tilde{a}_{\text{out}} = 4.5 \times 10^5$  AU = 2.2 pc. Since  $\tilde{a}_{\text{out}} \gg a$ , the octupole effects are negligible and have been

omitted in Eqs. (5–8). Note that these parameters give the same  $t_{\text{LK}}$  as Fig. 4 of LL18. We refer to this as the fiducial parameter regime, and our analysis in later sections will be based on this example unless otherwise noted.

We next discuss the key analytical properties of the orbital evolution.

### 2.1. Analytical Results Without GW Radiation

First, neglecting the GW radiation terms, the system admits two conservation laws, the “Kozai constant” and energy conservation,

$$j(e) \cos I = \text{const}, \quad (15)$$

$$\frac{3}{8} [2e^2 + j^2(e) \cos^2 I - 5e^2 \sin^2 I \sin^2 \omega] + \frac{\epsilon_{\text{GR}}}{j(e)} = \text{const}, \quad (16)$$

(see Anderson et al. 2016, LL18 for more general expressions when  $L_{\text{out}}$  is comparable to  $L$ ), where

$$\epsilon_{\text{GR}} \equiv (\Omega_{\text{GR}} t_{\text{LK}})_{e=0} = \frac{3Gm_{12}^2 \tilde{a}_{\text{out}}^3}{c^2 m_3 a^4}. \quad (17)$$

The conservation laws can be combined to obtain the maximum eccentricity  $e_{\text{max}}$  as a function of the initial  $I_i$  (and initial  $e_i \ll 1$ ). The largest value of  $e_{\text{max}}$  occurs at  $I_i = 90^\circ$  and is given by

$$j(e_{\text{max}})_{I_i=90^\circ} = (8/9)\epsilon_{\text{GR}}. \quad (18)$$

Eccentricity excitation then requires  $\epsilon_{\text{GR}} < 9/8$ . Our fiducial examples in Figs. 1 and 2 satisfy  $\epsilon_{\text{GR}} \ll 1$  at  $a = a_i$ , leading to  $e_{\text{max}} \sim 1$  within a narrow inclination window around  $I_i = 90^\circ$ .

Eqs. (15) and (16) imply that  $e$  is a function of  $\sin^2 \omega$  alone (see Kinoshita 1993; Storch & Lai 2015, for exact forms), so an eccentricity maximum occurs every half period of  $\omega$ . We define the period and angular frequency of eccentricity oscillation via

$$\pi = \int_0^{P_{\text{LK}}} \frac{d\omega}{dt} dt, \quad \Omega_{\text{LK}} \equiv \frac{2\pi}{P_{\text{LK}}}. \quad (19)$$

In LK cycles, the inner binary oscillates between the eccentricity minimum  $e_{\text{min}}$  and maximum  $e_{\text{max}}$ . The oscillation is “uneven”: when  $e_{\text{min}} \ll e_{\text{max}}$ , the binary spends a fraction  $\sim j(e_{\text{max}})$  of the LK cycle, or time  $\Delta t \sim t_{\text{LK}} j(e_{\text{max}})$ , near  $e \simeq e_{\text{max}}$  [see Eq. (8)].

### 2.2. Behavior with GW Radiation

Including the effect of GW radiation, orbital decay predominantly occurs at  $e \simeq e_{\text{max}}$  with the timescale of  $t_{\text{GW}}(e_{\text{max}})$  [see Eq. (14)]. On the other hand, Eq. (8) implies that, when  $\epsilon_{\text{GR}} \ll 1$ , the binary spends only a small fraction ( $\sim j(e_{\text{max}})$ ) of the time near  $e \simeq e_{\text{max}}$ . Thus, we expect two qualitatively different merger behaviors:

- “Rapid mergers”: When  $t_{\text{GW}}(e_{\text{max}}) \lesssim t_{\text{LK}}j(e_{\text{max}})$ , the binary is “pushed” into high eccentricity and exhibits a “one shot merger” without any  $e$ -oscillations.
- “Smooth mergers”: When  $t_{\text{GW}}(e_{\text{max}}) \gtrsim t_{\text{LK}}j(e_{\text{max}})$ , the binary goes through a phase of eccentricity oscillations while the orbit gradually decays. In this case, the LK-averaged orbital decay rate is  $\sim j(e_{\text{max}})t_{\text{GW}}^{-1}(e_{\text{max}})$ . As  $a$  decreases,  $e_{\text{max}}$  decreases slightly while the minimum eccentricity increases, approaching  $e_{\text{max}}$  (see Fig. 1). This eccentricity oscillation “freeze” ( $e_{\text{min}} \sim e_{\text{max}}$ ) is due to GR-induced apsidal precession ( $\epsilon_{\text{GR}}$  increases as  $a$  decreases), and occurs when  $\epsilon_{\text{GR}}(a) \gg j(e_{\text{max}})$ . After the eccentricity is frozen, the binary circularizes and decays on the timescale  $t_{\text{GW}}(e_{\text{max}})$ .

### 3. SPIN DYNAMICS: EQUATIONS

We are interested in the spin orientations of the inner BHs at merger as a function of initial conditions. Since they evolve independently to leading post-Newtonian order, we focus on the dynamics of  $\hat{\mathbf{S}}_1 = \hat{\mathbf{S}}$ , the spin vector of  $m_1$ . Since the spin magnitude does not enter into the dynamics, we write  $\mathbf{S} \equiv \hat{\mathbf{S}}$  for brevity (i.e.  $\mathbf{S}$  is a unit vector). Neglecting spin-spin interactions,  $\mathbf{S}$  undergoes de Sitter precession about  $\mathbf{L}$  as

$$\frac{d\mathbf{S}}{dt} = \Omega_{\text{SL}} \hat{\mathbf{L}} \times \mathbf{S}, \quad (20)$$

with

$$\Omega_{\text{SL}} = \frac{3Gn(m_2 + \mu/3)}{2c^2 a j^2(e)}. \quad (21)$$

In the presence of a tertiary companion, the orbital axis  $\hat{\mathbf{L}}$  of the inner binary precesses around  $\hat{\mathbf{L}}_{\text{out}}$  with rate  $d\varphi/dt$  and nutates with varying  $I$  [see Eqs. (6) and (72)]. To analyze the dynamics of the spin vector, we go to the co-rotating frame with  $\hat{\mathbf{L}}$  about  $\hat{\mathbf{L}}_{\text{out}}$ , in which Eq. (20) becomes

$$\left( \frac{d\mathbf{S}}{dt} \right)_{\text{rot}} = \mathbf{\Omega}_e \times \mathbf{S}, \quad (22)$$

where we have defined an effective rotation vector

$$\mathbf{\Omega}_e \equiv \Omega_{\text{L}} \hat{\mathbf{L}}_{\text{out}} + \Omega_{\text{SL}} \hat{\mathbf{L}}, \quad (23)$$

with [see Eq. (6)]

$$\Omega_{\text{L}} \equiv -\frac{d\varphi}{dt}. \quad (24)$$

In this rotating frame, the plane spanned by  $\hat{\mathbf{L}}_{\text{out}}$  and  $\hat{\mathbf{L}}$  is constant in time, only the inclination angle  $I$  can vary.

#### 3.1. Nondissipative Dynamics

We first consider the limit where dissipation via GW radiation is completely neglected ( $t_{\text{GW}}(e) \rightarrow \infty$ ). Then  $\mathbf{\Omega}_e$  is exactly periodic with period  $P_{\text{LK}}$  [see Eq. (19)] We can rewrite Eq. (22) in Fourier components

$$\left( \frac{d\mathbf{S}}{dt} \right)_{\text{rot}} = \left[ \bar{\mathbf{\Omega}}_e + \sum_{N=1}^{\infty} \mathbf{\Omega}_{eN} \cos(N\Omega_{\text{LK}}t) \right] \times \mathbf{S}. \quad (25)$$

We write  $\bar{\mathbf{\Omega}}_e \equiv \mathbf{\Omega}_{e0}$  for convenience, where the bar denotes an average over a LK cycle. We have adopted the convention where  $t = 0$  is the time of maximum eccentricity of the LK cycle, so that Eq. (25) does not have  $\sin(N\Omega_{\text{LK}}t)$  terms.

This system superficially resembles that considered in Storch & Lai (2015) (SL15), who studied the dynamics of the spin axis of a star when driven by a giant planet undergoing LK oscillations (see also Storch et al. 2014, 2017). In their system, the spin-orbit coupling arises from Newtonian interaction between the planet ( $M_p$ ) and the rotation-induced stellar quadrupole ( $I_{\text{out}} - I_1$ ), and the spin precession frequency is

$$\Omega_{\text{SL}}^{(\text{Newtonian})} = -\frac{3GM_p(I_{\text{out}} - I_1) \cos \theta_{\text{sl}}}{2a^3 j^3(e) I_3 \Omega_s}, \quad (26)$$

where  $I_3 \Omega_s$  is the spin angular momentum of the star. SL15 showed that under some conditions that depend on a dimensionless adiabaticity parameter (roughly the ratio between the magnitudes of  $\Omega_{\text{SL}}^{(\text{Newtonian})}$  and  $\Omega_{\text{L}}$  when factoring out the eccentricity and obliquity dependence), the stellar spin axis can vary chaotically. One strong indicator of chaos in their study is the presence of irregular, fine structure in a bifurcation diagram [Fig. 1 of Storch & Lai (2015)] that shows the values of the spin-orbit misalignment angle  $\theta_{\text{sl}}$  when varying system parameters in the “transadiabatic” regime, where the adiabaticity parameter crosses unity.

To generate an analogous bifurcation diagram for our problem, we consider a sample system with  $m_{12} = 60M_{\odot}$ ,  $m_3 = 3 \times 10^7 M_{\odot}$ ,  $a = 0.1$  AU,  $e_i = 10^{-3}$ ,  $I_i = 70^\circ$ ,  $a_{\text{out}} = 300$  AU,  $e_{\text{out}} = 0$ , and initial  $\theta_{\text{sl}} = 0$ . We then evolve Eq. (22) together with the orbital evolution equations [Eqs. (4–8) without the GW terms] while sampling both  $\theta_{\text{sl}}$  and  $\theta_e$  at eccentricity maxima, where  $\theta_e$  is given by

$$\cos \theta_e = \frac{\bar{\mathbf{\Omega}}_e}{\Omega_e} \cdot \mathbf{S}. \quad (27)$$

We repeat this procedure with different mass ratios  $m_1/m_{12}$  of the inner binary, which only changes  $\Omega_{\text{SL}}$  without changing the orbital evolution (note that the LK oscillation depends only on  $m_{12}$  and not on individual masses of the inner binary). Analogous to SL15, we consider systems with a range of the adiabaticity parameter  $\mathcal{A}$  [to be defined later in Eq. (31)] that

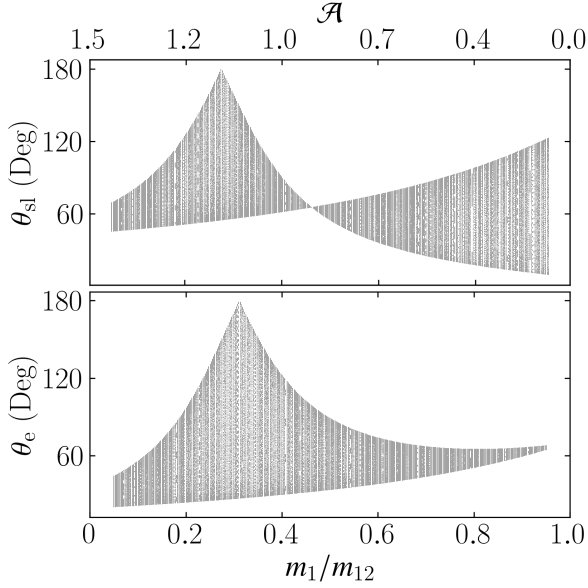


**Figure 3.** Bifurcation diagram for the BH spin orientation during LK oscillations. The physical parameters are  $m_{12} = 60M_{\odot}$ ,  $m_3 = 3 \times 10^7 M_{\odot}$ ,  $a = 0.1$  AU,  $e_i = 10^{-3}$ ,  $I_i = 70^\circ$ ,  $a_{\text{out}} = 300$  AU,  $e_{\text{out}} = 0$ , and initial condition  $\theta_{\text{sl},i} = 0$ . For each mass ratio  $m_1/m_{12}$ , the orbit-spin system is solved over 500 LK cycles, and both  $\theta_{\text{sl}}$  (the angle between  $\mathbf{S}$  and  $\hat{\mathbf{L}}$ ) and  $\theta_e$  [defined by Eq. (27)] are sampled at every eccentricity maximum and are plotted. The top axis shows the adiabaticity parameter  $\mathcal{A}$  as defined by Eq. (31). Note that for a given  $m_{12}$ , changing the mass ratio  $m_1/m_{12}$  only changes the spin evolution and not the orbital evolution.

crosses order unity. The fiducial system of Fig. 1 does not serve this purpose because the initial  $\Omega_{\text{SL}}$  is too small. Our result is depicted in Fig. 3.

While our bifurcation diagram has interesting structure, the features are all regular. This is in contrast to the star-planet system studied by SL15 (see their Fig. 1). A key difference is that in our system,  $\Omega_{\text{SL}}$  does not depend on  $\theta_{\text{sl}}$ , while for the planet-star system,  $\Omega_{\text{SL}}^{(\text{Newtonian})}$  does, and this latter feature introduces nonlinearity to the dynamics.

A more formal understanding of the dynamical behavior of our spin-orbit system comes from Floquet theory (Floquet 1883; Chicone 2006), as Eq. (22) is a linear system with periodic coefficients (the system studied in SL15 is nonlinear). Floquet’s theorem says that when a linear system with periodic coefficients is integrated over a period, the evolution can be described by the linear transformation

$$\mathbf{S}(t + P_{\text{LK}}) = \tilde{\mathbf{M}}\mathbf{S}(t), \quad (28)$$

where  $\tilde{\mathbf{M}}$  is called the *monodromy matrix* and is independent of  $\mathbf{S}$ .

For our system, while  $\tilde{\mathbf{M}}$  can be easily defined, it cannot be evaluated in closed form. Thankfully, it suffices to reason directly about the general properties of  $\tilde{\mathbf{M}}$ : it must be a proper

orthogonal matrix, or a rotation matrix, as it represents the effect of many infinitesimal rotations, each about the instantaneous  $\Omega_e$ <sup>1</sup>. Therefore, over each period  $P_{\text{LK}}$ , the dynamics of  $\mathbf{S}$  are equivalent to a rotation about a fixed axis, prohibiting chaotic behavior.

Another traditional indicator of chaos is a positive Lyapunov exponent, obtained when the separation between nearby trajectories diverges *exponentially* in time. In Floquet theory, the Lyapunov exponent is the logarithm of the largest eigenvalue of the monodromy matrix. Since  $\tilde{\mathbf{M}}$  is a rotation matrix in our problem, the Lyapunov exponent must be 0, indicating no chaos. We have verified this numerically.

### 3.2. Spin Dynamics With GW Dissipation

When  $t_{\text{GW}}$  is finite, the coefficients  $\Omega_{eN}$ , including  $\bar{\Omega}_e = \Omega_{e0}$  [see Eq. (25)], are no longer constant, but change over time. For “smooth” mergers (satisfying  $t_{\text{GW}}(e_{\text{max}}) \gg t_{\text{LK}}j(e_{\text{max}})$ ; see Section 2), the binary goes through a sequence of LK cycles, and the coefficients vary on the LK-averaged orbital decay time  $t_{\text{GW}}(e_{\text{max}})/j(e_{\text{max}})$ . As the LK oscillation freezes, we have  $\Omega_e \simeq \bar{\Omega}_e$  (and  $\Omega_{eN} \simeq 0$  for  $N \geq 1$ ), which evolves on timescale  $t_{\text{GW}}(e)$  as the orbit decays and circularizes.

Once  $a$  is sufficiently small such that  $\Omega_{\text{SL}} \gg \Omega_L$  (this also corresponds to  $\epsilon_{\text{GR}} \gg 1$  since  $\Omega_{\text{SL}} \sim \Omega_{\text{GR}}$ , implying the LK cycles are suppressed), it can be seen from Eqs. (22–23) that  $\theta_e = \theta_{\text{sl}}$  is constant, i.e. the spin-orbit misalignment angle is frozen (see bottom right panel of Fig. 1). This is the “final” spin-orbit misalignment, although the binary may still be far from the final merger. For the fiducial examples depicted in Figs. 1–2, we stop the simulation at  $a = 0.5$  AU, as  $\theta_{\text{sl}}$  has converged to its final value.

### 3.3. Spin Dynamics Equation in Component Form

For later analysis, it is useful to write Eq. (25) in component form. To do so, we define inclination angle  $\bar{I}_e$  as the angle between  $\bar{\Omega}_e$  and  $\mathbf{L}_{\text{out}}$  as shown in Fig. 4. To express  $\bar{I}_e$  algebraically, we define LK-averaged quantities

$$\overline{\Omega_{\text{SL}} \sin \bar{I}} \equiv \bar{\Omega}_{\text{SL}} \sin \bar{I}, \quad \overline{\Omega_{\text{SL}} \cos \bar{I}} \equiv \bar{\Omega}_{\text{SL}} \cos \bar{I}. \quad (29)$$

It then follows from Eq. (23) that

$$\tan \bar{I}_e = \frac{\mathcal{A} \sin \bar{I}}{1 + \mathcal{A} \cos \bar{I}}, \quad (30)$$

where  $\mathcal{A}$  is the adiabaticity parameter, given by

$$\mathcal{A} \equiv \frac{\bar{\Omega}_{\text{SL}}}{\Omega_L}. \quad (31)$$

<sup>1</sup> More formally,  $\tilde{\mathbf{M}} = \tilde{\Phi}(P_{\text{LK}})$  where  $\tilde{\Phi}(t)$  is the *principal fundamental matrix solution*: the columns of  $\tilde{\Phi}$  are solutions to Eq. (22) and  $\tilde{\Phi}(0)$  is the identity. By linearity, the columns of  $\tilde{\Phi}(t)$  remain orthonormal, while its determinant does not change, so  $\tilde{\mathbf{M}}$  is a proper orthogonal matrix, or a rotation matrix.



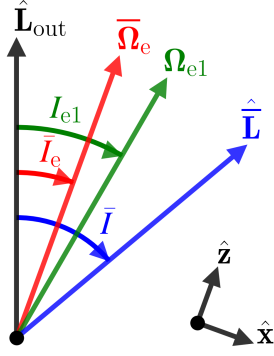


**Figure 4.** Definition of angles in the problem, shown in plane of the two angular momenta  $\mathbf{L}_{\text{out}}$  and  $\mathbf{L}$ . Here,  $\bar{\mathbf{L}}$  is the suitably averaged  $\mathbf{L}$  with inclination  $\bar{I}$  defined by Eq. (29),  $\bar{\Omega}_e$  is the LK-averaged  $\Omega_e$ , and  $\Omega_{e1}$  is the first harmonic component (see Eqs. (23) and (25)). Note that for  $I_i > 90^\circ$  (and  $\bar{I} > 90^\circ$ ), we choose  $\bar{I}_e \in (90^\circ, 180^\circ)$  so that  $\bar{\Omega}_e > 0$  (since  $\Omega_L < 0$ ). The bottom right shows our choice of coordinate axes with  $\hat{\mathbf{z}} \propto \bar{\Omega}_e$ .

Note that in Eq. (30),  $\bar{I}_e$  is defined in the domain  $[0^\circ, 180^\circ]$ , i.e.  $\bar{I}_e \in (0, 90)$  when  $\tan \bar{I}_e > 0$  and  $\bar{I}_e \in (90, 180)$  when  $\tan \bar{I}_e < 0$ .

We now choose a non-inertial coordinate system where  $\hat{\mathbf{z}} \propto \bar{\Omega}_e$  and  $\hat{\mathbf{x}}$  lies in the plane of  $\mathbf{L}_{\text{out}}$  and  $\mathbf{L}$  (see Fig. 4). In this reference frame, the spin orientation is specified by the polar angle  $\bar{\theta}_e$  as defined above in Eq. (36), and the equation of motion becomes

$$\left( \frac{d\mathbf{S}}{dt} \right)_{\text{xyz}} = \left[ \bar{\Omega}_e \hat{\mathbf{z}} + \sum_{N=1}^{\infty} \Omega_{eN} \cos(N\Omega_{LK}t) \right] \times \mathbf{S} - \dot{I}_e \hat{\mathbf{y}} \times \mathbf{S}. \quad (32)$$

One further simplification lets us cast this vector equation of motion into a scalar form. Break  $\mathbf{S}$  into components  $\mathbf{S} = S_x \hat{\mathbf{x}} + S_y \hat{\mathbf{y}} + \cos \bar{\theta}_e \hat{\mathbf{z}}$  and define complex variable

$$S_{\perp} \equiv S_x + iS_y. \quad (33)$$

Then, we can rewrite Eq. (32) as

$$\frac{dS_{\perp}}{dt} = i\bar{\Omega}_e S_{\perp} - \dot{I}_e \cos \bar{\theta}_e + \sum_{N=1}^{\infty} \left[ \cos(\Delta I_{eN}) S_{\perp} - i \cos \bar{\theta}_e \sin(\Delta I_{eN}) \right] \Omega_{eN} \cos(N\Omega_{LK}t), \quad (34)$$

where  $\Omega_{eN}$  is the magnitude of the vector  $\Omega_{eN}$  [see Eq. (25)] and  $\Delta I_{eN} = I_{eN} - \bar{I}_e$  where  $I_{eN}$  is the angle between  $\Omega_{eN}$  and  $\mathbf{L}_{\text{out}}$  (see Fig. 4).

#### 4. ANALYSIS: APPROXIMATE ADIABATIC INVARIANT

In general, Eqs. (25) and (34) are difficult to study analytically. In this section, we neglect the harmonic terms and focus on how the varying  $\bar{\Omega}_e$  affects the evolution of the BH spin axis. The effect of the harmonic terms is studied in Section 5.

##### 4.1. The Adiabatic Invariant

When neglecting the  $N \geq 1$  harmonic terms, Eq. (25) reduces to

$$\left( \frac{d\bar{\mathbf{S}}}{dt} \right)_{\text{rot}} = \bar{\Omega}_e \times \bar{\mathbf{S}}. \quad (35)$$

It is not obvious to what extent the analysis of Eq. (35) is applicable to Eq. (25). From our numerical calculations, we find that the LK-average of  $\mathbf{S}$  often evolves following Eq. (35), motivating our notation  $\bar{\mathbf{S}}$ . Over timescales shorter than the LK period  $P_{LK}$ , Eq. (35) loses accuracy as the evolution of  $\mathbf{S}$  itself is dominated by the  $N \geq 1$  harmonics we have neglected. An intuitive interpretation of this result is that the  $N \geq 1$  harmonics vanish when integrating Eq. (25) over a LK cycle.

Eq. (35) has one desirable property:  $\bar{\theta}_e$ , given by

$$\cos \bar{\theta}_e \equiv \frac{\bar{\Omega}_e}{\Omega_e} \cdot \bar{\mathbf{S}}, \quad (36)$$

is an adiabatic invariant. The adiabaticity condition requires the precession axis evolve slowly compared to the precession frequency at all times, i.e.

$$\left| \frac{d\bar{I}_e}{dt} \right| \ll \bar{\Omega}_e. \quad (37)$$

For our fiducial example depicted in Fig. 1, the values of  $\dot{I}_e$  and  $\bar{\Omega}_e$  are shown in the top panel of Fig. 5, and the evolution of  $\bar{\theta}_e$  in the bottom panel. The net change in  $\bar{\theta}_e$  in this simulation is  $0.01^\circ$ , small as expected since  $\left| \dot{I}_e \right| \ll \bar{\Omega}_e$  at all times.

##### 4.2. Deviation from Adiabaticity

The extent to which  $\bar{\theta}_e$  is conserved depends on how well Eq. (37) is satisfied. In this subsection, we derive a bound on the total non-conservation of  $\bar{\theta}_e$ , then in the next subsection we show how this bound can be estimated from initial conditions.

When neglecting harmonic terms, the scalar equation of motion Eq. (34) becomes

$$\frac{dS_{\perp}}{dt} = i\bar{\Omega}_e S_{\perp} - \dot{I}_e \cos \bar{\theta}_e. \quad (38)$$

This can be solved in closed form. Defining

$$\Phi(t) \equiv \int_0^t \bar{\Omega}_e dt, \quad (39)$$

we obtain the solution between the initial time  $t_i$  and the final time  $t_f$ :

$$e^{-i\Phi} S_{\perp} \Big|_{t_i}^{t_f} = - \int_{t_i}^{t_f} e^{-i\Phi(\tau)} \dot{I}_e \cos \bar{\theta}_e d\tau. \quad (40)$$

Recalling  $|S_\perp| = \sin \bar{\theta}_e$  and analyzing Eq. (40), we see that  $\bar{\theta}_e$  oscillates about its initial value with amplitude

$$|\Delta \bar{\theta}_e| \sim \left| \frac{\dot{\bar{I}}_e}{\bar{\Omega}_e} \right|. \quad (41)$$

In the adiabatic limit [Eq. (37)],  $\bar{\theta}_e$  is indeed conserved, as the right-hand side of Eq. (41) goes to zero. The bottom panel of Fig. 5 shows  $\Delta \bar{\theta}_e$  for the fiducial example. Note that  $\bar{\theta}_e$  is indeed mostly constant where Eq. (41) predicts small oscillations.

If we denote  $|\Delta \bar{\theta}_e|_f$  to be the net change in  $\bar{\theta}_e$  over  $t \in [t_i, t_f]$ , we can give a loose bound

$$|\Delta \bar{\theta}_e|_f \lesssim \left| \frac{\dot{\bar{I}}_e}{\bar{\Omega}_e} \right|_{\max}. \quad (42)$$

Inspection of Fig. 5 indicates that the spin dynamics are mostly uninteresting except near the peak of  $|\dot{\bar{I}}_e|$ , which occurs where  $\bar{\Omega}_{SL} \simeq |\Omega_L|$ . We present a zoomed-in view of dynamical quantities near the peak of  $\dot{\bar{I}}_e$  in Fig. 6. In particular, in the bottom-rightmost panel, we see that the fluctuations in  $\bar{\theta}_e$  are dominated by a second contribution, the subject of the discussion in Section 5.

For comparison, we show in Fig. 7 a more rapid binary merger starting with  $I_i = 90.2^\circ$ , for which  $|\Delta \theta_e|_f \approx 2^\circ$ . If we again examine the bottom-rightmost panel, we see that the net  $|\Delta \bar{\theta}_e|_f$  obeys Eq. (42).

#### 4.3. Estimate of Deviation from Adiabaticity from Initial Conditions

To estimate Eq. (42) as a function of initial conditions, we first differentiate Eq. (30),

$$\dot{\bar{I}}_e = \left( \frac{\dot{\mathcal{A}}}{\mathcal{A}} \right) \frac{\mathcal{A} \sin \bar{I}}{1 + 2\mathcal{A} \cos \bar{I} + \mathcal{A}^2}. \quad (43)$$

It also follows from Eq. (23) that

$$\bar{\Omega}_e = |\bar{\Omega}_L| \left( 1 + 2\mathcal{A} \cos \bar{I} + \mathcal{A}^2 \right)^{1/2}, \quad (44)$$

from which we obtain

$$\left| \frac{\dot{\bar{I}}_e}{\bar{\Omega}_e} \right| = \left( \frac{\dot{\mathcal{A}}}{\mathcal{A}} \right) \frac{1}{|\bar{\Omega}_L|} \frac{\mathcal{A} \sin \bar{I}}{(1 + 2\mathcal{A} \cos \bar{I} + \mathcal{A}^2)^{3/2}}. \quad (45)$$

Moreover, if we assume the eccentricity is frozen around  $e \simeq 1$  and use  $\cos^2 \omega \simeq 1/2$  in  $|\Omega_L| = |d\varphi/dt|$ , we obtain the estimate

$$\begin{aligned} \mathcal{A} &\simeq \frac{3Gn(m_2 + \mu/3)}{2c^2 a j^2(e)} \left[ \frac{15 \cos \bar{I}}{8 t_{LK} j(e)} \right]^{-1} \\ &\simeq \frac{4}{5} \frac{G(m_2 + \mu/3) m_{12} \tilde{a}_{\text{out}}^3}{c^2 m_3 a^4 j(e) \cos \bar{I}}, \end{aligned} \quad (46)$$

$$\frac{\dot{\mathcal{A}}}{\mathcal{A}} = -4 \left( \frac{\dot{a}}{a} \right)_{\text{GW}} + \frac{e}{j^2(e)} \left( \frac{de}{dt} \right)_{\text{GW}}. \quad (47)$$

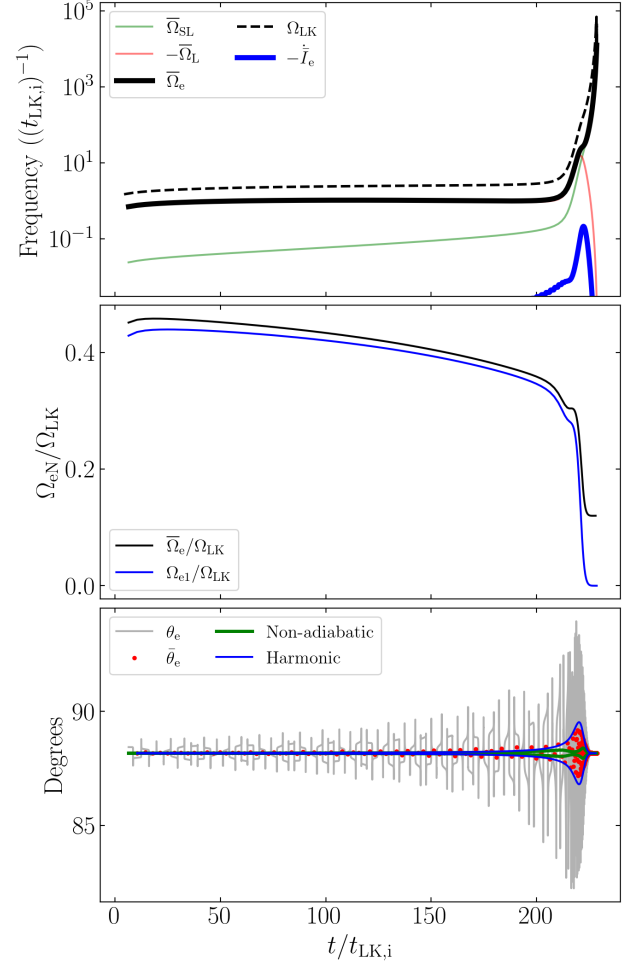


**Figure 5.** The same simulation as depicted in Fig. 1 but showing the calculated quantities relevant to the theory of the spin evolution. Top: the four characteristic frequencies of the system and  $d\bar{I}_e/dt$ . Middle: the frequency ratios between the zeroth and first Fourier components of  $\Omega_e$  to the LK frequency  $\Omega_{LK}$ . Bottom: Time evolution of  $\theta_e$  [grey line; Eq. (27)],  $\bar{\theta}_e$  [red dots; Eq. (36)], as well as estimates of the deviations from perfect conservation of  $\bar{\theta}_e$  due to nonadiabaticity [green, Eq. (41)] and due to resonances with the  $N = 1$  harmonic [blue, Eq. (67)].

With these, we see that Eq. (45) is largest around  $\mathcal{A} \simeq 1$ , and so we find that the maximum  $|\dot{\bar{I}}_e|/\bar{\Omega}_e$  is given by

$$\left| \frac{\dot{\bar{I}}_e}{\bar{\Omega}_e} \right|_{\max} \simeq \left| \frac{\dot{\mathcal{A}}}{\mathcal{A}} \right| \frac{1}{|\bar{\Omega}_L|} \frac{\sin \bar{I}}{(2 + 2 \cos \bar{I})^{3/2}}. \quad (48)$$

To evaluate this, we make two assumptions: (i)  $\bar{I}$  is approximately constant (see the third panels of Figs. 6 and 7), and (ii)  $j(e)$  evaluated at  $\mathcal{A} \simeq 1$  can be approximated as a constant multiple of the initial  $j(e_{\max})$ , i.e.

$$j_\star \equiv j(e_\star) = f \sqrt{\frac{5}{3} \cos^2 I_i}, \quad (49)$$

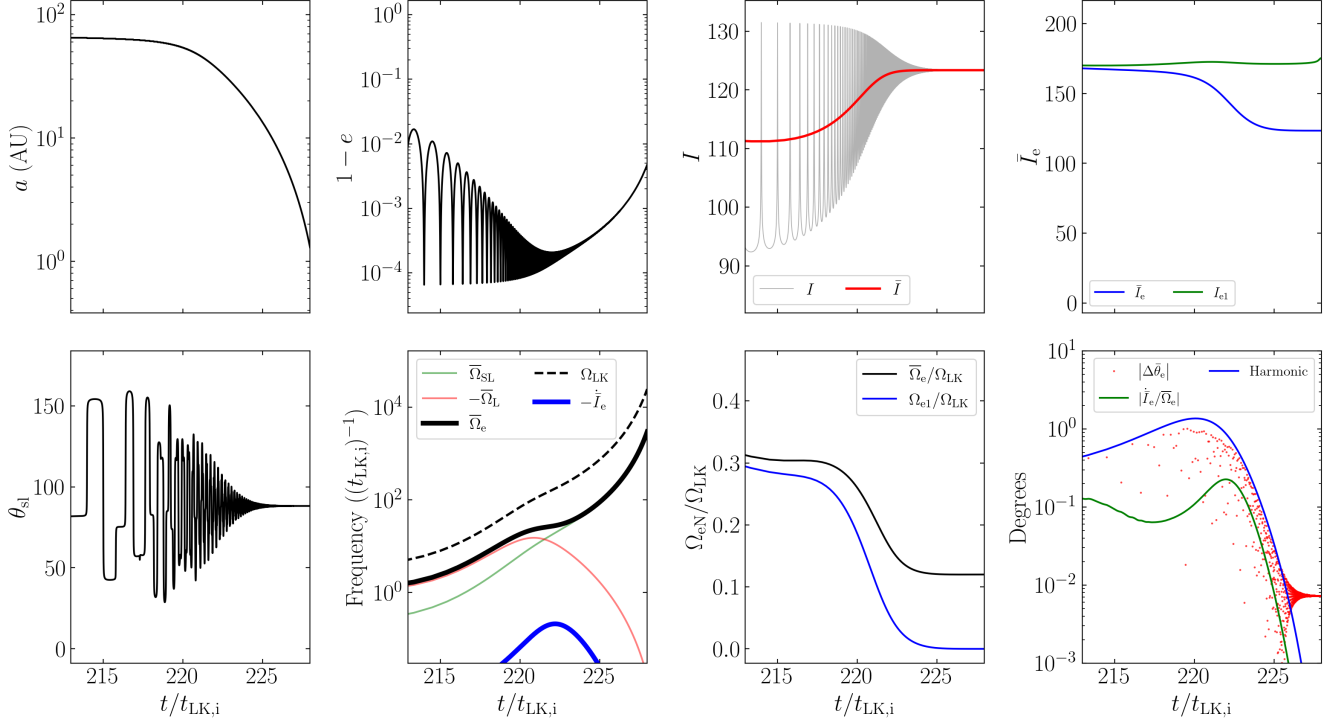


**Figure 6.** The same simulation as Fig. 1 but zoomed in on the region around  $\mathcal{A} \equiv \bar{\Omega}_{\text{SL}}/\bar{\Omega}_{\text{L}} \simeq 1$  and showing a wide range of relevant quantities. The first three panels in the upper row depict  $a$ ,  $e$ ,  $I$  and  $\bar{I}$  as in Fig. 1, while the fourth shows  $\bar{I}_e$  [Eq. (30)] and  $I_{e1}$ . The bottom four panels depict  $\theta_{\text{sl}}$ , the four characteristic frequencies of the system and  $d\bar{I}_e/dt$  [Eqs. 23 and (24)] (as in the top panel of Fig. 5), the relevant frequency ratios (as in the middle panel of Fig. 5), and the deviation of  $\bar{\theta}_e$  from its initial value compared to the predictions of Eqs. (41) and (67).

where the star subscript denotes evaluation at  $\mathcal{A} \simeq 1$  and  $f > 1$  is a constant. Eq. (49) assumes that  $I_i$  far enough from  $90^\circ$  that the GR effect is unimportant in determining  $e_{\text{max}}$ . The value of  $f$  turns out to be relatively insensitive to  $I_i$ .

Using Eq. (47) and approximating  $e_\star \approx 1$  in Eqs. (12) and (13) give

$$\left[ \frac{\dot{\mathcal{A}}}{\mathcal{A}} \right]_\star \simeq \frac{G^3 \mu m_{12}^2}{c^5 a_\star^4 j_\star^7} \frac{595}{3}. \quad (50)$$

To determine  $a_\star$ , we require Eq. (46) to give  $\mathcal{A} = 1$  for  $a_\star$  and  $j_\star$ . Taking this and Eq. (50), we rewrite Eq. (45) as

$$\left| \frac{\dot{\bar{I}}_e}{\bar{\Omega}_e} \right|_{\text{max}} \simeq \frac{595 \sin \bar{I} |\cos \bar{I}|^{3/8}}{36 (\cos \bar{I} + 1)^{3/2}} \left[ \frac{8000 G^9 m_{12}^9 m_3^3 \mu^8}{\bar{a}_{\text{out}}^9 j_\star^{37} c^{18} (m_2 + \mu/3)^{11}} \right]^{1/8}. \quad (51)$$

We can also calculate  $|\dot{\bar{I}}_e|/\bar{\Omega}_e$  from numerical simulations. Taking characteristic  $\bar{I} \approx 120^\circ$  (Figs. 6 and 7 show that this holds across a range of  $I_i$ ), we fit the last remaining free parameter  $f$  [Eq. (49)] to the data from numerical simulations.

This yields  $f \approx 2.72$ , leading to

$$\begin{aligned} \left| \frac{\dot{\bar{I}}_e}{\bar{\Omega}_e} \right|_{\text{max}} &\simeq 0.98^\circ \left( \frac{\cos I_i}{\cos(90.3^\circ)} \right)^{-37/8} \left( \frac{\bar{a}_{\text{out}}}{2.2 \text{ pc}} \right)^{-9/8} \\ &\times \left( \frac{m_3}{3 \times 10^7 M_\odot} \right)^{3/8} \left( \frac{m_{12}^9 \mu^8 / (m_2 + \mu/3)^{11}}{(28.64 M_\odot)^6} \right)^{1/8}. \end{aligned} \quad (52)$$

Fig. 8 shows that when the merger time  $T_m$  is much larger than the initial LK timescale, Eq. (52) provides an accurate estimate for  $|\dot{\bar{I}}_e/\bar{\Omega}_e|_{\text{max}}$  when compared with numerical results.

In the above, we have assumed that the system evolves through  $\mathcal{A} \simeq 1$  when the eccentricity is mostly frozen (see Fig. 1 for an indication of how accurate this is for the parameter space explored in Fig. 8). It is also possible that  $\mathcal{A} \simeq 1$  occurs when the eccentricity is still undergoing substantial oscillations. In fact, Eq. (52) remains accurate in this case when replacing  $e$  with  $e_{\text{max}}$ , due to the following analysis. Recall that when  $e_{\text{min}} \ll e_{\text{max}}$ , the binary spends a fraction  $\sim j(e_{\text{max}})$  of the LK cycle near  $e \simeq e_{\text{max}}$ . This fraction of the LK cycle dominates both GW dissipation and  $\bar{\Omega}_e$  precession. Thus, both  $\dot{\bar{I}}_e$  and  $\bar{\Omega}_e$  in the oscillating- $e$  regime can be evaluated by setting  $e \approx e_{\text{max}}$  and multiplying by a prefactor



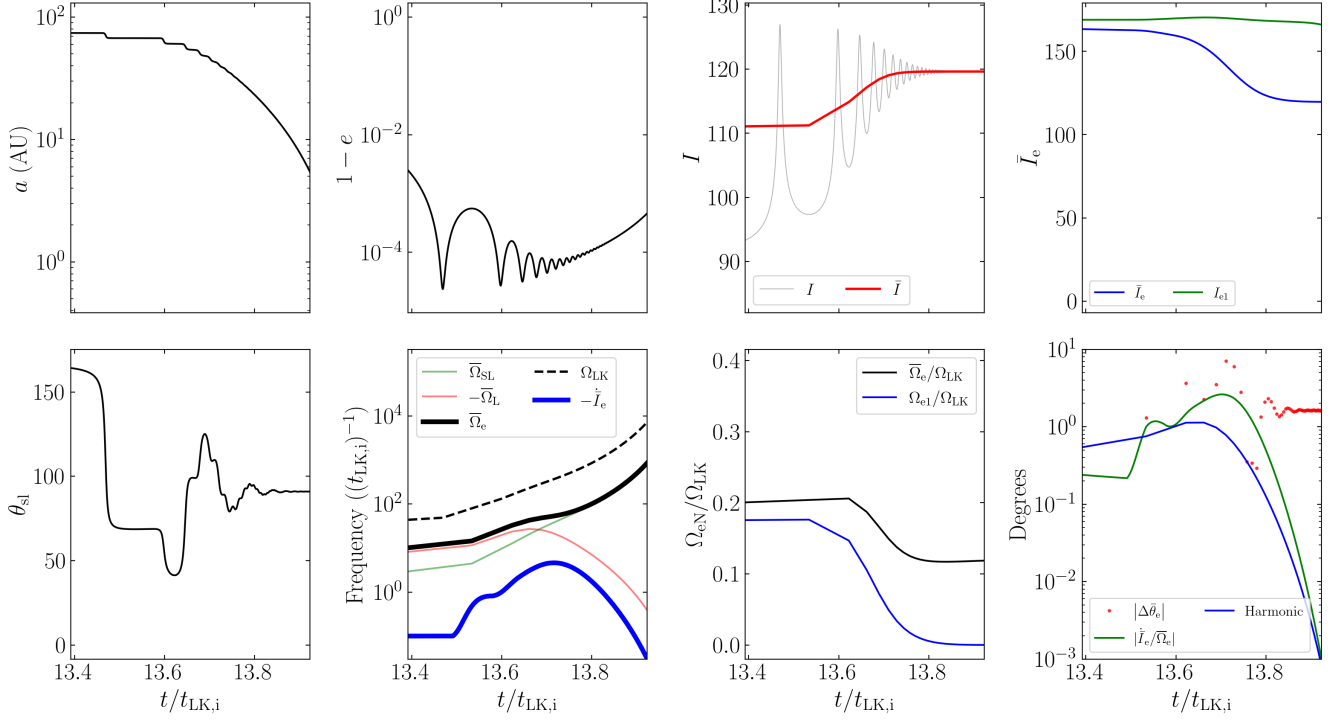


**Figure 7.** Same as Fig. 6 except for  $I_i = 90.2^\circ$  (and all other parameters are the same as in Fig. 1), corresponding to a faster coalescence. The total change in  $\bar{\theta}_e$  for this simulation is  $\approx 2^\circ$ .

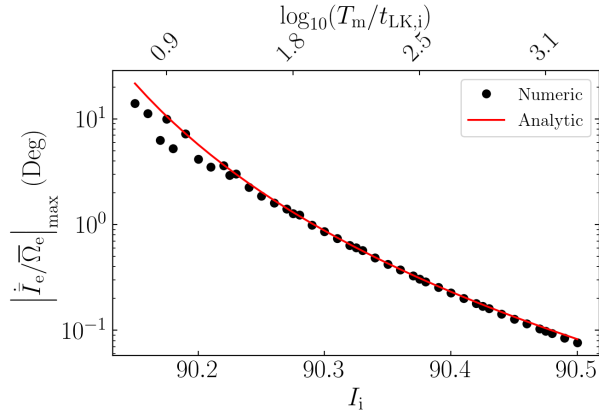


**Figure 8.** Comparison of  $|\dot{I}_e/\bar{\Omega}_e|_{\max}$  obtained from simulations and from the analytical expression Eq. (52), where we take  $f = 2.72$  in Eq. (49). The coalescence time  $T_m$  is shown along the top axis of the plot in units of the characteristic LK timescale at the start of inspiral  $t_{LK,i}$ . The agreement between the analytical and numerical results is excellent for  $T_m \gg t_{LK,i}$ .

of  $j(e_{\max})$ . This factor cancels when computing the quotient  $|\dot{I}_e|/\bar{\Omega}_e$ .

The accuracy of Eq. (52) in bounding  $|\Delta\bar{\theta}_e|_f$  is shown in Fig. 9, where we carry out simulations for a range of  $I_i$ , and for each  $I_i$  we consider 100 different, isotropically distributed

initial orientations for  $\mathbf{S}$  (thus sampling a wide range of initial  $\bar{\theta}_e$ ). Note that conservation of  $\bar{\theta}_e$  is generally much better than Eq. (52) predicts. This is because cancellation of phases in Eq. (40) is generally more efficient than Eq. (52) assumes (recall that Eq. (41) only provides an estimate for the amplitude of “local” oscillations of  $\bar{\theta}_e$ ). Nevertheless, it is clear that Eq. (52) provides a robust upper bound of  $|\Delta\bar{\theta}_e|_f$ , and serves as a good indicator for the breakdown of adiabatic invariance.

#### 4.4. Origin of the $\theta_{sl,f} = 90^\circ$ Attractor

Using the approximate adiabatic invariant, we can now understand the origin of the  $\theta_{sl,f} = 90^\circ$  attractor as shown in Fig. 2.

Recall from Eq. (23)

$$\begin{aligned}\bar{\Omega}_e &= \bar{\Omega}_L \hat{\mathbf{L}}_{\text{out}} + \bar{\Omega}_{SL} \hat{\mathbf{L}}, \\ &= (\bar{\Omega}_L + \bar{\Omega}_{SL} \cos \bar{I}) \hat{\mathbf{Z}} + \bar{\Omega}_{SL} \sin \bar{I} \hat{\mathbf{X}},\end{aligned}\quad (53)$$

where  $\hat{\mathbf{Z}} = \hat{\mathbf{L}}_{\text{out}}$  and  $\hat{\mathbf{X}}$  is perpendicular to  $\hat{\mathbf{Z}}$  in the  $\hat{\mathbf{L}}_{\text{out}}-\hat{\mathbf{L}}$  plane. Note that

$$\bar{\Omega}_L \propto \frac{\cos \bar{I}}{t_{LK}} \propto a^{3/2} \cos \bar{I}, \quad (54)$$

$$\bar{\Omega}_{SL} \propto \frac{1}{a^{5/2}}. \quad (55)$$

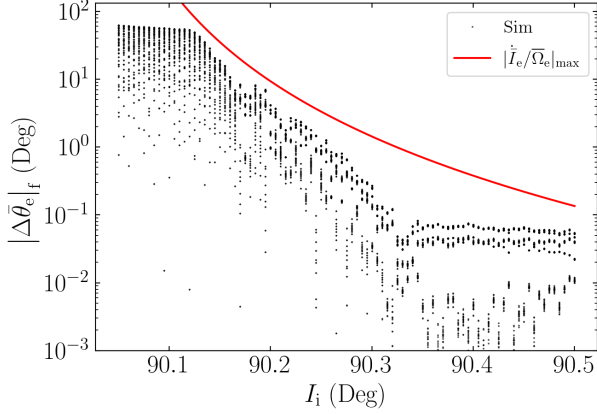


**Figure 9.** Net change in  $\bar{\theta}_e$  over the binary inspiral as a function of initial inclination  $I_i$ . For each  $I_i$ , 100 simulations are run for  $\mathbf{S}$  on a uniform, isotropic grid. Plotted for comparison is the bound  $|\Delta\bar{\theta}_e|_f \lesssim |\dot{I}_e/\bar{\Omega}_e|_{\max}$ , using the analytical expression given by Eq. (52). It is clear that the expression provides a robust upper bound for the non-conservation of  $\bar{\theta}_e$  due to nonadiabatic effects. Note that at the right of the plot, the numerical  $|\Delta\bar{\theta}_e|_f$  saturates; this is because we compute the initial  $\bar{\Omega}_e$  (in order to evaluate the initial  $\bar{\theta}_e$ ) without GW dissipation, and such a procedure inevitably introduces fuzziness in  $\bar{\theta}_e$ .

Adiabatic invariance implies that  $\bar{\theta}_e$ , the angle between  $\mathbf{S}$  and  $\bar{\Omega}_e$  is conserved between  $t = t_i$  and  $t = t_f$ , i.e.

$$\bar{\theta}_{e,f} \simeq \bar{\theta}_{e,i}. \quad (56)$$

At  $t = t_f$ ,  $\bar{\Omega}_{\text{SL}} \gg |\bar{\Omega}_L|$  and the spin-orbit misalignment angle  $\theta_{\text{sl}}$  is “frozen”, implying  $\bar{\Omega}_e$  is parallel to  $\mathbf{L}$ , and so  $\bar{\theta}_{e,f} = \theta_{\text{sl},f}$ . Eq. (56) then gives

$$\theta_{\text{sl},f} \simeq \bar{\theta}_{e,i}, \quad (57)$$

i.e. the final  $\theta_{\text{sl}}$  is determined by the initial angle between  $\mathbf{S}$  and  $\bar{\Omega}_e$ .

Now, first consider the case where the initial spin  $\mathbf{S}_i$  is aligned with the initial  $\mathbf{L}_i$ . This initial spin is inclined with respect to  $\bar{\Omega}_e$  by  $\bar{\theta}_{e,i} = |I_i - \bar{I}_{e,i}|$ , where  $I_i$  is the initial inclination angle between  $\mathbf{L}$  and  $\mathbf{L}_{\text{out}}$  and  $\bar{I}_{e,i}$  is the initial value of  $\bar{I}_e$ . Thus, adiabatic invariance implies

$$\theta_{\text{sl},f} \simeq |I_i - \bar{I}_{e,i}|. \quad (58)$$

In the special case where the binary initially satisfies  $\bar{\Omega}_{\text{SL}} \ll |\bar{\Omega}_L|$  or  $|\mathcal{A}_i| \ll 1$ , we find that  $\bar{\Omega}_e$  is nearly parallel to  $\mathbf{L}_{\text{out}}$  (for  $I_i < 90^\circ$ ) or antiparallel to  $\mathbf{L}_{\text{out}}$  (for  $I_i > 90^\circ$ ). Thus,

$$\theta_{\text{sl},f} = \begin{cases} I_i & I_i < 90^\circ, \\ 180^\circ - I_i & I_i > 90^\circ. \end{cases} \quad (59)$$

Since LK-induced mergers necessarily require  $I_i$  close to  $90^\circ$ , we find that  $\theta_{\text{sl},f}$  is “attracted” to  $90^\circ$ .

Eq. (57) can be applied to more general initial spin orientations. For initial  $|\mathcal{A}_i| \ll 1$  (as required for LK-induced mergers),  $\bar{\Omega}_{e,i}$  is parallel to  $\pm \mathbf{L}_{\text{out}}$ . Suppose the initial inclination between  $\mathbf{S}$  and  $\mathbf{L}_{\text{out}}$  is  $\theta_{\text{s-out},i}$ , then  $\bar{\theta}_{e,i} = \theta_{\text{s-out},i}$  or  $180^\circ - \theta_{\text{s-out},i}$  (depending on whether  $I_i < 90^\circ$  or  $I_i > 90^\circ$ ). Thus,

$$\theta_{\text{sl},f} \simeq \begin{cases} \theta_{\text{s-out},i} & I_i < 90^\circ, \\ 180^\circ - \theta_{\text{s-out},i} & I_i > 90^\circ, \end{cases} \quad (60)$$

(see also Yu et al. 2020).

So far, we have analyzed the  $\theta_{\text{sl},f}$  distribution for smooth mergers. Next, we can consider rapid mergers, for which  $\bar{\theta}_e$  conservation is imperfect. We expect

$$|\theta_{\text{sl},f} - \bar{\theta}_{e,i}| \lesssim |\Delta\bar{\theta}_e|_f. \quad (61)$$

where  $|\Delta\bar{\theta}_e|_f$  is given by Eq. (52). This is shown as the black dotted line in Fig. 2, and we see it predicts the maximum deviation of  $\theta_{\text{sl},f}$  from  $\sim 90^\circ$  except very near  $I_i = 90^\circ$ . This is expected, as Eq. (52) is not very accurate very near  $I_i = 90^\circ$ , where it diverges (see Fig. 9).

When  $I_i = 90^\circ$  exactly, Fig. 2 shows that  $\theta_{\text{sl},f} = 0^\circ$ . This can be understood:  $I_i = 90^\circ$  gives  $dI/dt = 0$  by Eq. (72), so  $I = 90^\circ$  for all time. This then implies  $d\mathcal{O}/dt = 0$  [Eq. (6)], implying that  $\mathbf{L}$  is constant. Thus,  $\mathbf{L}$  is fixed as  $\mathbf{S}$  precesses around it, and  $\theta_{\text{sl}}$  can never change. In Fig. 2, we take  $\theta_{\text{sl},i} = 0$ , so  $\theta_{\text{sl},f} = 0$ .

Finally, Fig. 2 shows that the actual  $\theta_{\text{sl},f}$  are oscillatory within the envelope bounded by Eq. (61) above. This can also be understood: Eq. (42) only bounds the maximum of the absolute value of the change in  $\bar{\theta}_e$ , while the actual change depends on the initial and final complex phases of  $S_\perp$  in Eq. (40), denoted  $\Phi(t_i)$  and  $\Phi(t_f)$ . When  $\theta_{\text{sl},i} = 0$ , we have  $\Phi(t_i) = 0$ , as  $\mathbf{S}$  starts in the  $\hat{\mathbf{x}}\text{-}\hat{\mathbf{z}}$  plane. Then, as  $I_i$  is smoothly varied, the final phase  $\Phi(t_f)$  must also vary smoothly [since  $\bar{\Omega}_e$  in Eq. (39) is a continuous function,  $\Phi(t)$  must be as well], so the total phase difference between the initial and final values of  $S_\perp$  varies smoothly. This means the total change in  $\bar{\theta}_e$  will fluctuate smoothly between  $\pm |\Delta\bar{\theta}_e|_f$  as  $I_i$  is changed, giving rise to the sinusoidal shape seen in Fig. 2.

## 5. ANALYSIS: EFFECT OF RESONANCES

In the previous section, we neglected the  $N \geq 1$  Fourier harmonics in Eq. (25), and showed that the final  $\theta_{\text{sl},f}$  behavior could be well understood. In this section, we study the effects of the Fourier harmonics. We argue that the harmonics can be neglected for the fiducial parameter regime. A regime for which the Fourier harmonics cannot be neglected is discussed separately in Section 6.

For simplicity, we ignore the effects of GW dissipation in this section and assume the system is exactly periodic (so

$\dot{I}_e = 0$ ). The scalar equation of motion Eq. (34) is then:

$$\frac{dS_{\perp}}{dt} = i\bar{\Omega}_e S_{\perp} + \sum_{N=1}^{\infty} \left[ \cos(\Delta I_{eN}) S_{\perp} - i \cos \theta \sin(\Delta I_{eN}) \right] \Omega_{eN} \cos(N\Omega_{LK}t). \quad (62)$$

Resonances may occur when  $\bar{\Omega}_e = N\Omega_{LK}$ . Assuming the resonances do not overlap, we restrict our attention to a single harmonic at a time. There are then two time-dependent perturbations, a modulation of the oscillation frequency and a driving term. We analyze these two terms separately to identify resonant behaviors.

First, we consider the effect of frequency modulation alone. The equation of motion is

$$\frac{dS_{\perp}}{dt} \approx i\bar{\Omega}_e S_{\perp} + \cos(\Delta I_{eN}) \Omega_{eN} \cos(N\Omega_{LK}t) S_{\perp}. \quad (63)$$

This can be exactly solved, and we obtain

$$S_{\perp}(t) = S_{\perp}(t_i) \int_{t_i}^t \exp \left[ -i\bar{\Omega}_e - \cos(\Delta I_{eN}) \Omega_{eN} \cos(N\Omega_{LK}t) \right] dt. \quad (64)$$

The two terms in the integrand contribute separately to the phase and magnitude of  $S_{\perp}$  respectively, and it is evident there is no condition for which the magnitude of  $S_{\perp}$  can diverge. Thus, there are no resonances induced by this frequency modulation.

When considering only the time-dependent driving term instead, the equation of motion is

$$\frac{dS_{\perp}}{dt} \approx i\bar{\Omega}_e S_{\perp} - i \cos \bar{\theta}_e \sin(\Delta I_{eN}) \Omega_{eN} \cos(N\Omega_{LK}t). \quad (65)$$

We can approximate  $\cos(N\Omega_{LK}t) \approx e^{iN\Omega_{LK}t}/2$ , as the  $e^{-iN\Omega_{LK}t}$  component is far from resonance. Then we can write down solution as before

$$e^{-i\bar{\Omega}_e t} S_{\perp} \Big|_{t_i}^{t_f} = - \int_{t_i}^{t_f} \frac{i \sin(\Delta I_{eN}) \Omega_{eN}}{2} e^{-i\bar{\Omega}_e t + iN\Omega_{LK}t} \cos \bar{\theta}_e dt. \quad (66)$$

Thus, similarly to Section 4.2, the instantaneous oscillation amplitude  $|\Delta \bar{\theta}_e|$  can be bound by

$$|\Delta \bar{\theta}_e| \sim \frac{1}{2} \left| \frac{\sin(\Delta I_{eN}) \Omega_{eN}}{\bar{\Omega}_e - N\Omega_{LK}} \right|. \quad (67)$$

We see indeed that the oscillation amplitude diverges when  $\bar{\Omega}_e = N\Omega_{LK}$ . Numerically, we find that  $\bar{\Omega}_e < \Omega_{LK}$  for the relevant region of parameter space to LK-induced mergers (see Fig. 10, and recall that LK-induced mergers only complete within a Hubble time when  $I(e_{\min}) \approx 90^\circ$ ), so we consider

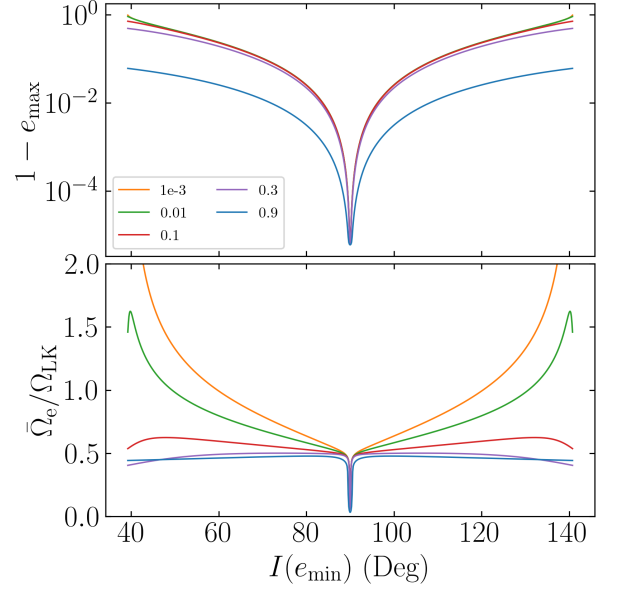


**Figure 10.**  $e_{\max}$  and  $\bar{\Omega}_e/\Omega_{LK}$  as a function of  $I(e_{\min})$ , the inclination of the inner binary at eccentricity minimum, for varying values of  $e_{\min}$  (different colors) for the fiducial parameter regime. In the fiducial parameter regime, where only systems with  $I_i \approx 90^\circ$  will merge within a Hubble time,  $I(e_{\min}) \sim 90^\circ$  for most of the evolution (see Fig. 1) until  $e_{\min} \approx 1$  is satisfied. This plot then shows that  $\bar{\Omega}_e \lesssim 0.5\Omega_{LK}$  is a general feature of LK-induced mergers, as is the case for the fiducial simulation (see Fig. 5).

only the  $N = 1$  resonance. We see that if  $\bar{\Omega}_e < \Omega_{LK}$  by a sufficient margin for all times, then the conservation of  $\bar{\theta}_e$  in the fiducial parameter regime cannot be significantly affected by this resonance. The ratio  $\bar{\Omega}_e/\Omega_{LK}$  is shown in the middle panel of Fig. 5, and the amplitude of oscillation of  $\bar{\theta}_e$  it generates [Eq. (67)] is given in blue in the bottom panel of Fig. 5. We see that the total effect of the resonance with the  $N = 1$  harmonic never exceeds a few degrees.

For a more precise comparison, the bottom-rightmost panel of Fig. 6 compares the behavior of  $\bar{\theta}_e$  to its two contributions, the nonadiabatic and harmonic effects, in the regime where  $\mathcal{A} \approx 1$ . We see that Eq. (67) for  $N = 1$  describes the oscillations in  $\bar{\theta}_e$  very well. The agreement is poorer in the bottom-rightmost panel of Fig. 7, as the nonadiabatic effect is much stronger. This is surprising, as the theory presented in the previous section, which neglects the Fourier harmonics, captures the final deviations  $|\Delta \bar{\theta}_e|_f$  very well (see Fig. 9 for  $I_i = 90.35^\circ$ ), despite the instantaneous  $|\Delta \bar{\theta}_e|$  being dominated by the resonance interaction. This suggests that oscillations in  $\bar{\theta}_e$  due to harmonic perturbations of up to a few degrees do not affect final nonconservation by more than  $\sim 0.01^\circ$ .

## 6. LIDOV-KOZAI ENHANCED MERGERS

We turn now to the case of LK-enhanced mergers, as was studied in LL17, where the inner binary is sufficiently close in ( $\sim 0.1$  AU) that it can merge in isolation via GW radiation. Here, we consider a similar set of parameters that has the same  $t_{\text{LK},i}$  as the system studied in LL17 but has a tertiary SMBH:  $m_1 = m_2 = 30M_\odot$ ,  $a_i = 0.1$  AU,  $e_i = 10^{-3}$ ,  $m_3 = 3 \times 10^7 M_\odot$ ,  $\tilde{a}_{\text{out}} = 3$  AU, and  $e_{\text{out}} = 0$ .

First, we illustrate the  $\theta_{\text{sl},f}$  distribution obtained via numerical simulation, shown as the blue dots in Fig. 11. The prediction assuming conservation of  $\bar{\theta}_e$  is shown in the red solid line. Good agreement is observed both when no eccentricity excitation occurs ( $I \lesssim 50^\circ$  and  $I \gtrsim 130^\circ$ ) and when  $|\mathcal{A}| \gg 1$ .

However, as can be seen in Fig. 11, intermediate inclinations  $I_i \in [50, 80]$  and  $I_i \in [100, 130]$  exhibit very volatile behavior in  $\theta_{\text{sl},f}$ . This is unlike the plots generated in the fiducial parameter regime (Fig. 2), as this inclination regime corresponds to neither the fastest nor slowest merging systems. We attribute the origin of this volatility to a stronger resonant interaction. Fig. 12 illustrates that these intermediate inclinations are closer to the  $\bar{\Omega}_e = \Omega_{\text{LK}}$  resonance than inclinations closer to  $90^\circ$ . Furthermore, as the inner binary coalesces under GW radiation,  $e_{\text{min}}$  becomes larger (e.g. see Fig. 1), so the locations of the resonances sweep outwards from  $I = 90^\circ$ . Moreover, the location of the resonances is a very sensitive function of  $e_{\text{min}}$  (see the results for  $e_{\text{min}} = 10^{-3}$  and  $e_{\text{min}} = 10^{-2}$  in Fig. 12), so resonance passage is generally expected to be nonadiabatic. Thus, we expect that all systems that encounter the resonance, i.e. all intermediate inclinations, will have poor conservation of  $\bar{\theta}_e$ . This is denoted by the broad red shaded region in Fig. 11 over these intermediate inclinations.

Instead, for inclinations closer to  $I_i = 90^\circ$ , these systems exit the resonance very early, and so the cumulative effect of the resonance interaction can be predicted by evaluating Eq. (67) for  $N = 1$  and using the initial conditions. This is denoted by the narrow red shaded region about the red line near  $I_i = 90^\circ$  in Fig. 11. We see that the scatter is well predicted for these weakly-resonant conditions. We empirically choose the transition between “weakly” and “strongly” resonant systems when the  $|\Delta\bar{\theta}_e|$  predicted by Eq. (67) exceeds  $7^\circ$ .

To understand the properties of systems that will interact strongly with resonances we can reason about the quantities in Eq. (67):

- $\sin(\Delta I_{\text{eN}})$  is small unless  $\mathcal{A} \simeq 1$ . Otherwise,  $\Omega_e$  does not nutate appreciably within a LK cycle, and all the  $\Omega_{\text{eN}}$  are aligned with  $\bar{\Omega}_e$ , implying all the  $\Delta I_{\text{eN}} \approx 0$ .
- Smaller values of  $e_{\text{min}}$  increase  $\bar{\Omega}_e/\Omega_{\text{LK}}$ , as shown in Fig. 12.

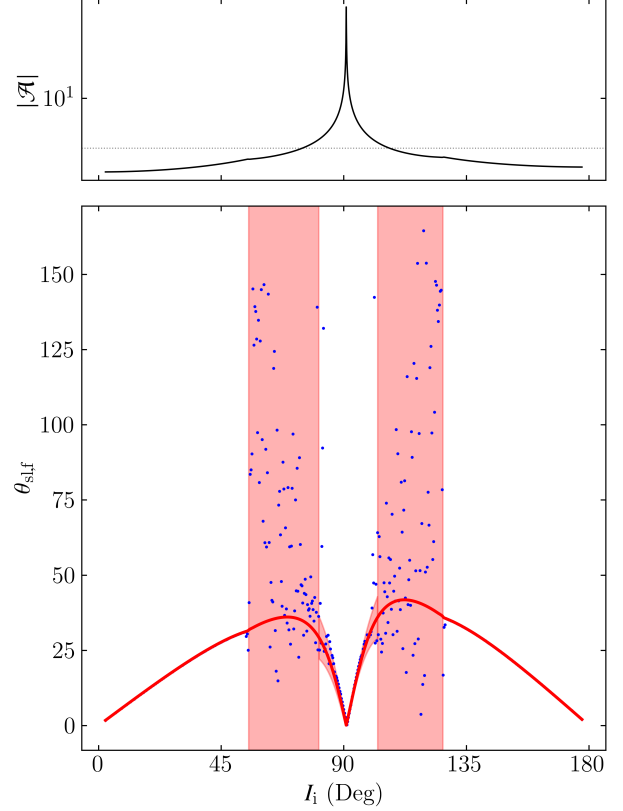


**Figure 11.** [TEMPORARILY USING FINITE ETA PLOT] Plot of the magnitude of the adiabaticity parameter  $|\mathcal{A}| \equiv \Omega_{\text{SL}}/|\Omega_{\text{L}}|$  and the final spin-orbit misalignment angle  $\theta_{\text{sl},f}$  for the LK-enhanced parameter regime, i.e.  $m_1 = m_2 = 30M_\odot$ ,  $m_3 = 3 \times 10^7 M_\odot$ ,  $a_i = 0.1$  AU,  $e_i = 10^{-3}$ ,  $\tilde{a}_{\text{out}} = 300$  AU, and  $e_{\text{out}} = 0$ . On the top panel, the horizontal dashed line indicates  $|\mathcal{A}| = 1$ . On the bottom panel, the blue dots denote results from numerical simulations with  $\theta_{\text{sl},f} = 0$ . The prediction for  $\theta_{\text{sl},f}$  assuming conservation of  $\theta_e$  is given the red line, which agrees well with the data both when there is no eccentricity excitation ( $I \lesssim 50^\circ$  and  $I \gtrsim 130^\circ$ ) and when  $|\mathcal{A}| \gg 1$ . The red shaded area shows the predicted deviation from conservation of  $\theta_e$ , given by Eq. (67) for  $N = 1$ . For a substantial range of intermediate inclinations ( $I \in [50^\circ, 80^\circ]$  and  $I \in [100^\circ, 130^\circ]$ ), the spin is significantly affected the resonances as they sweep outwards from  $I = 90^\circ$  (see Fig. 12). As such, these initial inclinations are expected to have largely uncorrelated  $\theta_{\text{sl},f}$  and  $\theta_{e,i}$ , and we denote this range with a broad red shaded interval.

However, LK-driven coalescence causes  $\mathcal{A}$  to increase on a similar timescale to that of  $e_{\text{min}}$  increase (see Fig. 1). This implies that, if  $\mathcal{A} \ll 1$  initially, which is the case for LK-induced mergers, then  $e_{\text{min}}$  will be very close to 1 when  $\mathcal{A}$  grows to be  $\simeq 1$ , and the contribution predicted by Eq. (67) will remain small throughout the entire evolution. On the other hand, if  $\mathcal{A} \simeq 1$  initially, as is the case for the intermediate inclinations in the LK-enhanced regime, resonant interactions can be significant.

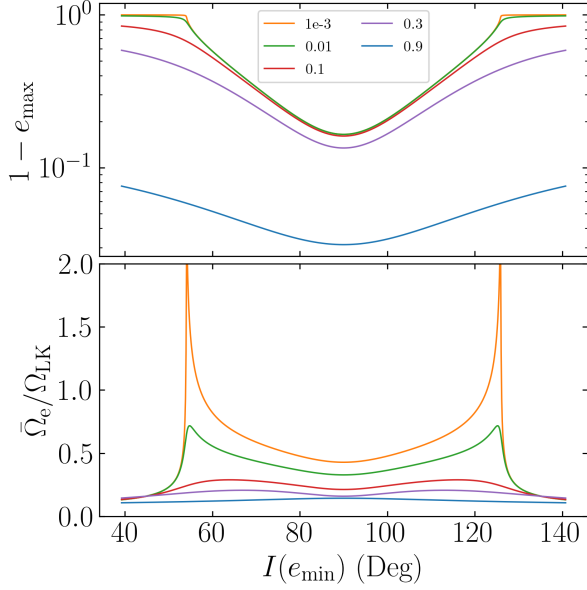


**Figure 12.** Same as Fig. 10 but for the LK-enhanced parameter regime. In the LK-enhanced regime, all  $I_i$  merge within a Hubble time, and it is clear that  $\bar{\Omega}_e \approx \Omega_{LK}$  can be satisfied for a wide range of inclinations. However,  $e_{\max} \lesssim 0.8$  for these inclinations is moderate compared to the LK-induced regime.

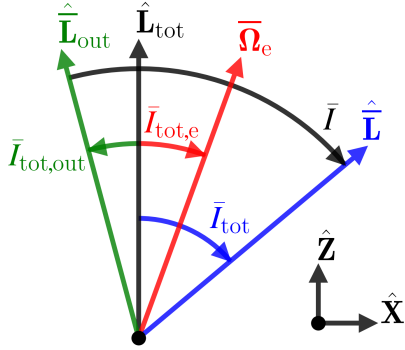


**Figure 13.** Definition of angles in the case where  $L/L_{\text{out}}$  is nonzero. Similar to before, we choose the convention where  $\bar{I}_{\text{tot},e} \in [0^\circ, 90^\circ]$  when  $\bar{\Omega}_L > 0$  and  $\bar{I}_{\text{tot},e} \in [90^\circ, 180^\circ]$  when  $\bar{\Omega}_L < 0$ . Here,  $\mathbf{L}_{\text{out}}$  is not fixed, but  $\mathbf{L}_{\text{tot}} \equiv \mathbf{L} + \mathbf{L}_{\text{out}}$  is. Note that the coordinate system is now oriented with  $\hat{\mathbf{Z}} \propto \mathbf{L}_{\text{tot}}$ .

## 7. STELLAR MASS BLACK HOLE TRIPLES

In this section, we extend our predictions for the final spin-orbit misalignment angle  $\theta_{\text{sl},f}$  to systems where all three masses are comparable and the ratio of the angular momenta of the two binaries

$$\eta \equiv \left. \frac{L}{L_{\text{out}}} \right|_{e=e_{\text{out}}=0} = \frac{\mu}{\mu_{\text{out}}} \left[ \frac{m_{12}a}{m_{123}a_{\text{out}}} \right]^{1/2}, \quad (68)$$

where  $m_{123} = m_{12} + m_3$  and  $\mu_{\text{out}} = m_{12}m_3/m_{123}$ , is not negligible. When  $\eta \neq 0$ ,  $\mathbf{L}_{\text{out}}$  is no longer fixed, but the total angular momentum  $\mathbf{L}_{\text{tot}} \equiv \mathbf{L} + \mathbf{L}_{\text{out}}$  is fixed. We choose the coordinate system with  $\hat{\mathbf{Z}} = \hat{\mathbf{L}}_{\text{tot}}$ , shown in Fig. 13.

To analyze this system, we still assume  $e_{\text{out}} \ll 1$  such that the octupole-order effects are negligible. To calculate the evolution of  $\mathbf{L}$ , it is only necessary to evolve a single orbital element for the outer binary, the inclination  $I_{\text{tot},\text{out}}$  relative to the total angular momentum, in addition to the orbital elements of the inner binary ( $a$ ,  $e$ ,  $\delta\Omega$ ,  $I_{\text{tot}}$ , and  $\omega$  as before), as the ascending node of the outer binary satisfies  $\delta\Omega_{\text{out}} = \delta\Omega + 180^\circ$ . The equations of motion are given by (Liu et al. 2015)

$$\frac{da}{dt} = \left( \frac{da}{dt} \right)_{\text{GW}}, \quad (69)$$

$$\frac{de}{dt} = \frac{15}{8t_{\text{LK}}} e j(e) \sin 2\omega \sin^2 I + \left( \frac{de}{dt} \right)_{\text{GW}}, \quad (70)$$

$$\frac{d\delta\Omega}{dt} = \frac{L_{\text{tot}}}{L_{\text{out}}} \frac{3}{4t_{\text{LK}}} \frac{\cos I (5e^2 \cos^2 \omega - 4e^2 - 1)}{j(e)}, \quad (71)$$

$$\frac{dI_{\text{tot}}}{dt} = -\frac{15}{16t_{\text{LK}}} \frac{e^2 \sin 2\omega \sin 2I}{j(e)}, \quad (72)$$

$$\frac{dI_{\text{tot},\text{out}}}{dt} = -\eta \frac{15}{8t_{\text{LK}}} (e^2 \sin 2\omega \sin I), \quad (73)$$

$$\begin{aligned} \frac{d\omega}{dt} = \frac{3}{t_{\text{LK}}} & \left\{ \frac{4 \cos^2 I + (5 \cos(2\omega) - 1)(1 - e^2 - \cos^2 I)}{8j(e)} \right. \\ & \left. + \frac{\eta \cos I}{8} [2 + e^2(3 - 5 \cos(2\omega))] \right\} + \Omega_{\text{GR}}, \end{aligned} \quad (74)$$

where  $I = I_{\text{tot}} + I_{\text{tot},\text{out}}$  is the relative inclination between the two angular momenta. The spin evolution of one of the inner BHs is then described in the corotating with  $\mathbf{L}$  about  $\mathbf{L}_{\text{tot}}$  by the equation of motion

$$\left( \frac{d\mathbf{S}}{dt} \right)_{\text{rot}} = \boldsymbol{\Omega}_e \times \mathbf{S}, \quad (75)$$

where

$$\begin{aligned} \boldsymbol{\Omega}_e & \equiv \Omega_{\text{SL}} \hat{\mathbf{L}} + \Omega_L \hat{\mathbf{L}}_{\text{tot}}, \\ & = \overline{\Omega_{\text{SL}}} \sin I_{\text{tot}} \hat{\mathbf{X}} + \left( \overline{\Omega_L} + \overline{\Omega_{\text{SL}}} \cos I_{\text{tot}} \right) \hat{\mathbf{Z}}, \end{aligned} \quad (76)$$

where  $\Omega_L = -d\delta\Omega/dt$  [Eq. (71)] is the rate of precession of  $\mathbf{L}$  about  $\mathbf{L}_{\text{tot}}$ , and bars denote averaging over an LK cycle. It is then natural to define the averaged quantities

$$\overline{\Omega_{\text{SL}}} \sin I_{\text{out}} \equiv \overline{\Omega_{\text{SL}}} \sin \bar{I}_{\text{out}}, \quad \overline{\Omega_{\text{SL}}} \cos I_{\text{out}} \equiv \overline{\Omega_{\text{SL}}} \cos \bar{I}_{\text{out}} \quad (77)$$

The results of Section 4 suggest that the angle  $\bar{\theta}_e$  is an adiabatic invariant, where  $\bar{\theta}_e$  is given by

$$\cos \bar{\theta}_e \equiv \frac{\bar{\Omega}_e}{\Omega_e} \cdot \bar{\mathbf{S}}. \quad (78)$$



The orientation of  $\bar{\Omega}_e$  is described by the inclination angle  $\bar{I}_{\text{tot},e}$  (Fig. 13), which can be expressed using Eq. (76)

$$\tan \bar{I}_{\text{tot},e} = \frac{\mathcal{A} \sin \bar{I}_{\text{tot}}}{1 + \mathcal{A} \cos \bar{I}_{\text{tot}}}, \quad (79)$$

where  $\mathcal{A} \equiv \bar{\Omega}_{\text{SL}}/\bar{\Omega}_{\text{L}}$  is the adiabaticity parameter.

At  $t = t_f$ , the inner binary has become sufficiently compact that  $\theta_{\text{sl}}$  becomes frozen (see bottom right panel of Fig. 1), and the system satisfies  $\mathcal{A} \gg 1$ , as  $\bar{\Omega}_{\text{SL}} \propto a^{-5/2}$  while  $\bar{\Omega}_{\text{L}} \propto a^{3/2}$ . When this is satisfied,  $\bar{\Omega}_e \parallel \mathbf{L}$ , and so  $\bar{\theta}_{e,f} = \theta_{\text{sl},f}$ . Then, since adiabatic invariance implies  $\bar{\theta}_{e,f} = \bar{\theta}_{e,i}$ ,

$$\theta_{\text{sl},f} = \bar{\theta}_{e,i}. \quad (80)$$

First, we consider the case where  $\mathbf{S}_i = \hat{\mathbf{L}}_i$ . Then  $\bar{\theta}_{e,i} = |I_{\text{tot},i} - \bar{I}_{\text{tot},e,i}|$  (see Fig. 13), and so

$$\theta_{\text{sl},f} = |I_{\text{tot},i} - \bar{I}_{e,i}|. \quad (81)$$

Suppose additionally that the binary initially satisfies  $|\bar{\Omega}_{\text{L}}| \gg \bar{\Omega}_{\text{SL}}$ , then  $\bar{\Omega}_e$  is either parallel or anti-parallel to  $\mathbf{L}_{\text{tot}}$  depending on whether  $\bar{\Omega}_{\text{L}}$  is positive or negative. Define  $I_c$  to be the starting mutual inclination for which  $\bar{\Omega}_{\text{L}}$  changes sign. Note that even though  $\Omega_{\text{L}}$  changes sign at  $I = 90^\circ$  [see Eq. (71)],  $I_c > 90^\circ$ . This is because for  $I < I_{\text{lim}}$ , where  $I_{\text{lim}} \approx 92.16^\circ$  is the starting mutual inclination that maximizes  $e_{\text{max}}$  (Liu & Lai 2018), the inclination can decrease to below  $90^\circ$  when the eccentricity increases. As such, we find that

$$\theta_{\text{sl},f} = \begin{cases} I_{\text{tot},i} & I_i < I_c, \\ 180^\circ - I_{\text{tot},i} & I_i > I_c. \end{cases} \quad (82)$$

More generally, so long as  $\mathcal{A} \ll 1$  initially, we can specify the initial spin orientation by  $\theta_{s,\text{tot},i}$ , the initial angle between  $\mathbf{S}$  and  $\mathbf{L}_{\text{tot}}$ , giving

$$\theta_{\text{sl},f} = \begin{cases} \theta_{s,\text{tot},i} & I < I_c, \\ 180^\circ - \theta_{s,\text{tot},i} & I > I_c. \end{cases} \quad (83)$$

We first compare these results to numerical simulations by considering a stellar-mass BH triple that is in the LK-induced regime: we use the same inner binary parameters as the fiducial system before, but use a tertiary companion with  $m_3 = 30M_\odot$ ,  $a_{\text{out}} = 4500$  AU, and  $e_{\text{out}} = 0$ . Again, we use the  $\theta_{\text{sl},i} = 0$ . Fig. 14 shows that Eq. (81) accurately predicts  $\theta_{\text{sl},f}$  for this parameter regime when conservation of  $\bar{\theta}_e$  is good. Furthermore, deviations from exact  $\bar{\theta}_e$  conservation are well described by Eq. (61), the prediction of the theory in Section 4. Unlike the  $\eta = 0$  case (Fig. 2),  $\theta_{\text{sl},f}$  is not symmetric about  $I_c \approx 92.14^\circ$ . This is because  $|\Omega_{\text{L}}|$  is not exactly equal on either side of  $I_c$ . Additionally, unlike in the

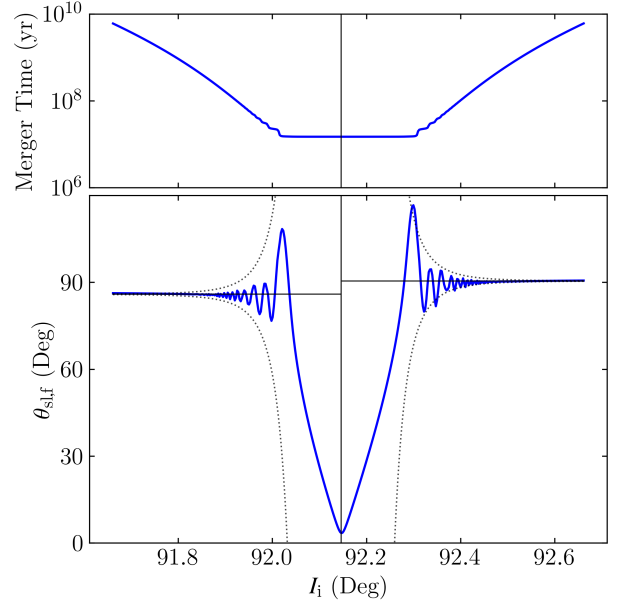


**Figure 14.** Similar to Fig. 2 but for stellar-mass tertiary  $m_3 = 30M_\odot$  and  $\bar{a}_3 = 4500$  AU. The vertical black line denotes  $I_c \approx 92.14^\circ$ , the inclination for which  $\bar{\Omega}_{\text{L}}$  changes signs, and the two horizontal lines denote the predictions of Eq. (81). The dotted black lines bound the deviation due to non-adiabatic evolution, given by Eq. (61).

$\eta = 0$  case, the minimum  $\theta_{\text{sl},f}$  is not exactly zero. We showed in Section 4.4 that when  $\eta = 0$ ,  $\mathbf{L}$  is fixed when  $I_i = 90^\circ$ , as  $d\Omega/dt = dI/dt = 0$ . For nonzero  $\eta$ ,  $d\Omega/dt$  and  $dI_{\text{tot}}/dt$  are not zero at  $I_i = I_c$ .

Eq. (81) also holds well over a large range of  $I_i$  in the LK-enhanced merger regime, as shown in Fig. 15. We see that shape of the  $\theta_{\text{sl},f}$  distribution near its minimum around  $I_i \approx 91.14^\circ$  is well captured.

## 8. CONCLUSION AND DISCUSSION

In this paper, we consider the evolution of the spin-orbit misalignment angle  $\theta_{\text{sl}}$  of a black hole (BH) binary that merges under gravitational wave (GW) radiation during Lidov-Kozai (LK) oscillations induced by a tertiary supermassive black hole (SMBH). We show that, when the SMBH orbit is circular and octupole effects are unimportant, the spin vectors of the inner BHs obey the simple equation of motion Eq. (22). Analysis of this equation yields the following conclusions:

- For most parameters of astrophysical relevance, the angle  $\bar{\theta}_e$  [Eq. (36)] is an adiabatic invariant. Since the inner BH binary merges in finite time,  $\bar{\theta}_e$  is only conserved to finite accuracy; we show that the deviation from perfect adiabaticity can be predicted from initial conditions.

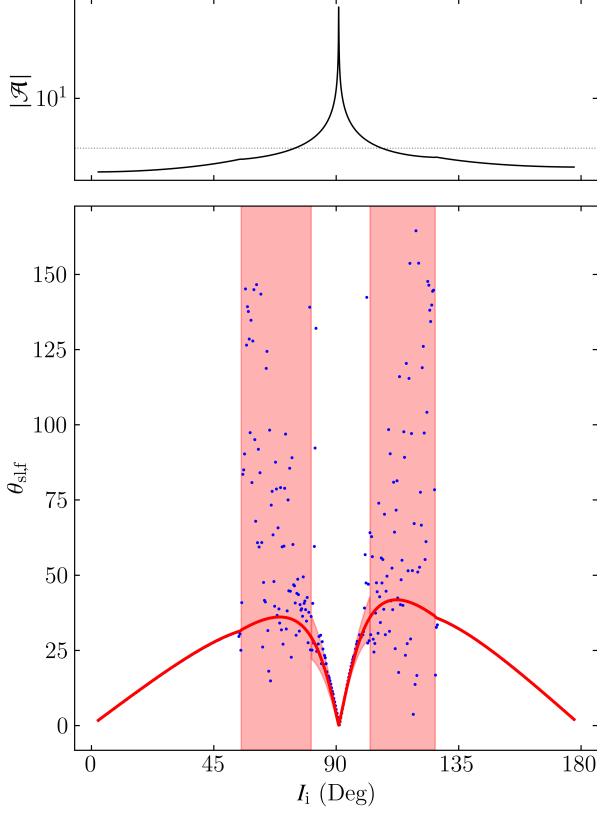


**Figure 15.** Similar to Fig. 11 except with stellar mass tertiary  $m_3 = 30M_\odot$  and  $\tilde{a}_{\text{out}} = 3$  AU.

- When the resonant condition  $\bar{\Omega}_e \approx \Omega_{\text{LK}}$  is satisfied, significant oscillations in  $\bar{\theta}_e$  can arise. We derive an analytic estimate of this oscillation amplitude. This es-

timate both demonstrates that the resonance is unimportant for “LK-induced” mergers and tentatively explains the scatter in  $\theta_{\text{sl},f}$  seen by LL17.

- These results can be generalized to stellar mass BH triples, for which our results are still accurate.

Possible discussion points:

- We see that the  $90^\circ$  attractor found in LL18 when the octupole effect is negligible is a result of the choosing the initial condition  $\theta_{\text{sl},i} = 0^\circ$ . In particular, the distribution of  $\theta_{\text{sl},f}$  is directly related to the distribution of  $\theta_{\text{sl},i}$  through the angle  $\bar{\theta}_{e,i}$ .
- When the tertiary orbit is eccentric, the octupole-order contributions can no longer be neglected. The octupole-order LK effect is no longer integrable, and the eccentricity excitations are no longer regular (see e.g. Liu & Lai 2018). In this case,  $\Omega_e$  has neither consistent direction nor magnitude, and the resulting  $\theta_{\text{sl},f}$  distribution is largely unrelated to the initial  $\bar{\theta}_{e,i}$  (Liu & Lai 2018).
- If the system is not sufficiently hierarchical ( $a_{\text{out}}$  is too small), the double averaging approximation breaks down, and the dynamics are no longer integrable, so there is little reason to expect the same relation between  $\theta_{\text{sl},f}$  and  $\bar{\theta}_{e,i}$ . However, Liu & Lai (2018) found that the double averaged equations predict the correct merger window and merger fractions even beyond their regime of validity if the octupole effect is weak, so it is possible that our results on  $\theta_{\text{sl},f}$  are somewhat robust even when the double averaged equations break down. We defer this possibility to future work.

## REFERENCES

- Abbott, B., et al. 2016, *Phys. Rev. Lett.*, 116, 061102, doi: [10.1103/PhysRevLett.116.061102](https://doi.org/10.1103/PhysRevLett.116.061102)
- Abbott, B., Abbott, R., Abbott, T., et al. 2019, *The Astrophysical Journal Letters*, 882, L24
- Abbott, R., Abbott, T., Abraham, S., et al. 2020, *The Astrophysical Journal Letters*, 900, L13
- Anderson, K. R., Storch, N. I., & Lai, D. 2016, *Monthly Notices of the Royal Astronomical Society*, 456, 3671
- Antonini, F., & Perets, H. B. 2012, *The Astrophysical Journal*, 757, 27
- Antonini, F., Rodriguez, C. L., Petrovich, C., & Fischer, C. L. 2018, *Monthly Notices of the Royal Astronomical Society: Letters*, 480, L58
- Antonini, F., Toonen, S., & Hamers, A. S. 2017, *The Astrophysical Journal*, 841, 77
- Banerjee, S., Baumgardt, H., & Kroupa, P. 2010, *Monthly Notices of the Royal Astronomical Society*, 402, 371
- Belczynski, K., Dominik, M., Bulik, T., et al. 2010, *The Astrophysical Journal Letters*, 715, L138
- Belczynski, K., Holz, D. E., Bulik, T., & O’Shaughnessy, R. 2016, *Nature*, 534, 512
- Belczynski, K., Klencki, J., Fields, C., et al. 2020, *Astronomy & Astrophysics*, 636, A104
- Blaes, O., Lee, M. H., & Socrates, A. 2002, *The Astrophysical Journal*, 578, 775
- Chicone, C. 2006, *Ordinary differential equations with applications*, Vol. 34 (Springer Science & Business Media)
- Dominik, M., Belczynski, K., Fryer, C., et al. 2012, *The Astrophysical Journal*, 759, 52

- . 2013, *The Astrophysical Journal*, 779, 72
- Dominik, M., Berti, E., O’Shaughnessy, R., et al. 2015, *The Astrophysical Journal*, 806, 263
- Downing, J., Benacquista, M., Giersz, M., & Spurzem, R. 2010, *Monthly Notices of the Royal Astronomical Society*, 407, 1946
- Floquet, G. 1883, in *Annales scientifiques de l’École normale supérieure*, Vol. 12, 47–88
- Gondán, L., Kocsis, B., Raffai, P., & Frei, Z. 2018, *The Astrophysical Journal*, 860, 5
- Hoang, B.-M., Naoz, S., Kocsis, B., Rasio, F. A., & Dosopoulou, F. 2018, *The Astrophysical Journal*, 856, 140
- Kinoshita, H. 1993, *Celestial Mechanics and Dynamical Astronomy*, 57, 359
- Lipunov, V., Postnov, K., & Prokhorov, M. 1997, *Astronomy Letters*, 23, 492
- Lipunov, V., Kornilov, V., Gorbovskoy, E., et al. 2017, *Monthly Notices of the Royal Astronomical Society*, 465, 3656
- Liu, B., & Lai, D. 2017, *The Astrophysical Journal Letters*, 846, L11
- . 2018, *The Astrophysical Journal*, 863, 68
- Liu, B., Lai, D., & Wang, Y.-H. 2019, *The Astrophysical Journal*, 881, 41
- Liu, B., Muñoz, D. J., & Lai, D. 2015, *Monthly Notices of the Royal Astronomical Society*, 447, 747
- Miller, M. C., & Hamilton, D. P. 2002, *The Astrophysical Journal*, 576, 894
- Miller, M. C., & Lauburg, V. M. 2009, *The Astrophysical Journal*, 692, 917
- O’leary, R. M., Rasio, F. A., Fregeau, J. M., Ivanova, N., & O’Shaughnessy, R. 2006, *The Astrophysical Journal*, 637, 937
- Podsiadlowski, P., Rappaport, S., & Han, Z. 2003, *Monthly Notices of the Royal Astronomical Society*, 341, 385
- Postnov, K., & Kuranov, A. 2019, *Monthly Notices of the Royal Astronomical Society*, 483, 3288
- Randall, L., & Xianyu, Z.-Z. 2018, *The Astrophysical Journal*, 853, 93
- Rodriguez, C. L., Amaro-Seoane, P., Chatterjee, S., & Rasio, F. A. 2018, *Physical Review Letters*, 120, 151101
- Rodriguez, C. L., Morscher, M., Pattabiraman, B., et al. 2015, *Physical Review Letters*, 115, 051101
- Samsing, J., & D’Orazio, D. J. 2018, *Monthly Notices of the Royal Astronomical Society*, 481, 5445
- Samsing, J., & Ramirez-Ruiz, E. 2017, *The Astrophysical Journal Letters*, 840, L14
- Schmidt, P., Ohme, F., & Hannam, M. 2015, *Physical Review D*, 91, 024043
- Shankar, R. 2012, *Principles of quantum mechanics* (Springer Science & Business Media)
- Silsbee, K., & Tremaine, S. 2016, arXiv preprint arXiv:1608.07642
- Storch, N. I., Anderson, K. R., & Lai, D. 2014, *Science*, 345, 1317
- Storch, N. I., & Lai, D. 2015, *Monthly Notices of the Royal Astronomical Society*, 448, 1821
- Storch, N. I., Lai, D., & Anderson, K. R. 2017, *Monthly Notices of the Royal Astronomical Society*, 465, 3927
- Wen, L. 2003, *The Astrophysical Journal*, 598, 419
- Yu, H., Ma, S., Giesler, M., & Chen, Y. 2020, arXiv preprint arXiv:2007.12978
- Ziosi, B. M., Mapelli, M., Branchesi, M., & Tormen, G. 2014, *Monthly Notices of the Royal Astronomical Society*, 441, 3703
- Zwart, S. F. P., & McMillan, S. L. 1999, *The Astrophysical Journal Letters*, 528, L17

## APPENDIX

## A. FLOQUET THEORY ANALYSIS

In this appendix, we show using a combination of analytical and numerical methods that the approximations made in the main text are accurate and completely describe the spin dynamics of the inner BH. We again work in the corotating frame and neglect GW dissipation, so the equation of motion is given by Eq. (22). If we define the matrix operator satisfying  $\tilde{\mathbf{A}}\mathbf{S} = \mathbf{\Omega}_e \times \mathbf{S}$ , i.e.  $\tilde{A}_{ik} = \epsilon_{ijk}\Omega_{e,j}$ , then the equation of motion is

$$\left(\frac{d\mathbf{S}}{dt}\right)_{\text{rot}} = \tilde{\mathbf{A}}(t)\mathbf{S}. \quad (\text{A1})$$

Here,  $\tilde{\mathbf{A}}$  is periodic with period  $T_{\text{LK}}$ .

## A.1. Without Nutation

First, for simplicity, let us first assume that  $\mathbf{\Omega}_e$  does not nutate significantly, so its orientation is fixed ( $\mathbf{\Omega}_e$  does not precess in the corotating frame, as the plane of  $\mathbf{L}$ – $\mathbf{L}_{\text{out}}$  is fixed). In this case, Eq. (A1) admits an exact conserved quantity:

$$\frac{d}{dt} [e^{-\Phi}\mathbf{S}] = 0, \quad (\text{A2})$$

where

$$\Phi(t) \equiv \int_0^t \tilde{\mathbf{A}} dt. \quad (\text{A3})$$

Separately, since Eq. (A1) is linear and has periodic coefficients, Floquet theory mandates that  $\mathbf{S}(t + T_{\text{LK}})$  be related to  $\mathbf{S}(t)$  by the monodromy matrix  $\tilde{\mathbf{M}}$  satisfying

$$\mathbf{S}(t + T_{\text{LK}}) = \tilde{\mathbf{M}}\mathbf{S}(t). \quad (\text{A4})$$

Comparing Eqs. (A2) and (A4), we immediately find that

$$\begin{aligned} \tilde{\mathbf{M}} &= \exp \left[ - \int_0^{T_{\text{LK}}} \tilde{\mathbf{A}} dt \right], \\ &= \exp \left[ -T_{\text{LK}} \overline{\tilde{\mathbf{A}}} \right], \end{aligned} \quad (\text{A5})$$

where again the overline denotes time averaging.

Now, we define a surrogate spin vector  $\mathbf{S}_{\text{surr}}$  that evolves as

$$\begin{aligned} \frac{d\mathbf{S}_{\text{surr}}}{dt} &= \overline{\tilde{\mathbf{A}}}\mathbf{S}_{\text{surr}}, \\ &= \overline{\mathbf{\Omega}}_e \times \mathbf{S}_{\text{surr}}. \end{aligned} \quad (\text{A6})$$

The evolution of  $\mathbf{S}_{\text{surr}}$  also obeys  $\mathbf{S}_{\text{surr}}(t + T_{\text{LK}}) = \tilde{\mathbf{M}}\mathbf{S}_{\text{surr}}(t)$ . This then implies that if  $\mathbf{S}_i = \mathbf{S}_{\text{surr},i}$ , then  $\mathbf{S} = \mathbf{S}_{\text{surr}}$  at every  $t = NT_{\text{LK}}$ .

When the system is allowed to evolve under GW radiation,  $\tilde{\mathbf{M}}$  evolves on the timescale  $t_{\text{GW}}$ . Furthermore, as the inner binary coalesces,  $T_{\text{LK}} \rightarrow 0$  and the variation of  $\tilde{\mathbf{A}}$  within  $T_{\text{LK}}$  vanishes (as LK oscillations freeze out). As such, we see that if  $t_{\text{GW}} \gg T_{\text{LK}}$ , i.e. the merger is smooth, the evolution of  $\mathbf{S}$  and the surrogate  $\mathbf{S}_{\text{surr}}$  are exactly equal for  $t = t_i + NT_{\text{LK}}$  and converge once the LK oscillations freeze out. This shows that studying the equation of motion Eq. (A6) for  $\mathbf{S}_{\text{surr}}$ , as is done in Section 4, gives an accurate prediction of the final spin  $\mathbf{S}_f$  when the merger is smooth and nutation of  $\mathbf{\Omega}_e$  within a LK period can be neglected.

## A.2. Effect of Nutation

In the previous section, we have assumed  $\mathbf{\Omega}_e$  does not nutate within a LK period. However, even for the fiducial example shown in Fig. 1, there are periods of time over which  $\mathbf{\Omega}_e$  nutates substantially within a LK period. In this section, our objective is to understand the conditions under which nutation can be neglected. To this end, we will work perturbatively by assuming that the nutation of  $\mathbf{\Omega}_e$  is small and seeking the breakdown of our solution.

When  $\mathbf{\Omega}_e$  is allowed to nutate within  $T_{\text{LK}}$ , the quantity given by Eq. (A2) is no longer conserved, as

$$\frac{d}{dt} [e^{-\Phi}\mathbf{S}] = e^{-\Phi} \frac{d\mathbf{S}}{dt} - \tilde{\mathbf{A}} e^{-\Phi} \mathbf{S} \neq e^{-\Phi} \left[ \frac{d\mathbf{S}}{dt} - \tilde{\mathbf{A}}\mathbf{S} \right] = 0. \quad (\text{A7})$$

Instead, we define new quantities  $\Phi'$  and  $\tilde{\mathbf{B}}$  defined such that

$$\Phi'(t) \equiv \int_0^t \tilde{\mathbf{A}} + \tilde{\mathbf{B}} dt, \quad (\text{A8})$$

$$\frac{d}{dt} [e^{-\Phi'}\mathbf{S}] = 0. \quad (\text{A9})$$

This requires

$$\tilde{\mathbf{B}} = [e^{-\Phi'}, \tilde{\mathbf{A}}] e^{\Phi'}, \quad (\text{A10})$$

where the square brackets denote the commutator. The monodromy matrix is then

$$\tilde{\mathbf{M}} = \exp \left[ - \int_0^{T_{\text{LK}}} \tilde{\mathbf{A}} + \tilde{\mathbf{B}} dt \right]. \quad (\text{A11})$$

We next want to understand when Eq. (A11) can be well approximated by Eq. (A5). From Eq. (A10), we see that  $\tilde{\mathbf{B}} = 0$  vanishes when  $[\tilde{\mathbf{A}}, \Phi]$  commute, which occurs when  $\mathbf{\Omega}_e$  does not nutate. However, a small range of nutation alone is not sufficient to guarantee Eq. (A11) is well approximated

by Eq. (A5). To see this, we expand the matrix exponential using the well known Baker-Campbell-Hausdorff formula (e.g. Shankar 2012)

$$\tilde{\mathbf{M}} = e^{-T_{\text{LK}}\bar{\mathbf{A}}} e^{-T_{\text{LK}}\bar{\mathbf{B}}} \exp \left[ \int_0^{T_{\text{LK}}} \frac{[\tilde{\mathbf{A}}, \tilde{\mathbf{B}}]}{2} + \dots dt \right]. \quad (\text{A12})$$

These matrix exponentials are rotation matrices, and the first rotation matrix  $e^{-T_{\text{LK}}\bar{\mathbf{A}}}$  rotates by total angle  $\bar{\Omega}_e T_{\text{LK}}$ , which for the problem considered in the main text is not more than a few times  $2\pi$  (see Figs. 10 and 12). On the other hand, if  $\bar{\mathbf{B}}$  is small by assumption,  $e^{-T_{\text{LK}}\bar{\mathbf{B}}}$  and the remaining matrices rotate by an angle  $\ll 2\pi$  and are very near the identity matrix. Therefore, if  $e^{-T_{\text{LK}}\bar{\mathbf{A}}}$  is not very near the identity matrix, then Eq. (A5) is approximately correct and the rotation axis of  $\tilde{\mathbf{M}}$  (call this  $\mathbf{R}$ ) is very nearly  $\bar{\Omega}_e$  as before.

However, if  $\bar{\Omega}_e T_{\text{LK}} \approx 2\pi N$  for integer  $N$ , then  $e^{-T_{\text{LK}}\bar{\mathbf{A}}}$  itself is near the identity as well, and the remaining matrices that depend on  $\bar{\mathbf{B}}$  cannot be neglected when calculating  $\mathbf{R}$ . As such, we conclude that even very small nutation of  $\Omega_e$  can change  $\mathbf{R}$  significantly when  $\bar{\Omega}_e \approx N\Omega_{\text{LK}}$ .

### A.3. Quantitative Effect

Above, we have given a qualitative analysis of the exact solution for the monodromy matrix  $\tilde{\mathbf{M}}$ . In this section, we aim to reconcile this with the quantitative, approximate results in the text and suggest that the results in the text constitute a complete characterization of the spin dynamics.

In Section 4 of the main text, we found that  $\mathbf{S}$  precesses around  $\bar{\Omega}_e$  when  $N \geq 1$  harmonics of the periodic  $\Omega_e$  are neglected, a result justified in Appendix A.1. In Section 5, we found that one effect of these  $N \geq 1$  harmonics are fluctuations in  $\bar{\theta}_e$  when  $\bar{\Omega}_e \approx N\Omega_{\text{LK}}$  with amplitude Eq. (67). On the other hand, in Appendix A.2, we found that  $\mathbf{R}$  is aligned with  $\bar{\Omega}_e$  except when  $\bar{\Omega}_e$  is sufficiently close to  $N\Omega_{\text{LK}}$  that nutation of  $\Omega_e$  becomes important, but we were not able to determine a quantitative criterion for the effect of nutation. In this section, we show numerically that the formulas given in the main text give good predictions for the orientation of  $\mathbf{R}$ .

To validate the analytic prediction given by Eq. (67), we numerically compute  $\tilde{\mathbf{M}}$ . We study the  $\eta \neq 0$ , LK-enhanced regime. We still neglect GW dissipation in order for Floquet analysis to be applicable. For 2000 different initial inclinations of the inner binary, we construct  $\tilde{\mathbf{M}}$  by evolving the spin equation of motion Eq. (22) starting with the three initial conditions  $\mathbf{S} = \hat{\mathbf{x}}$ ,  $\mathbf{S} = \hat{\mathbf{y}}$ , and  $\mathbf{S} = \hat{\mathbf{z}}$  (see Fig. 16) over a single LK period, then using

$$\tilde{\mathbf{M}} = \Phi(T_{\text{LK}}) \Phi^{-1}(0) = \Phi(T_{\text{LK}}), \quad (\text{A13})$$

where  $\Phi(t)$  is the *principal fundamental matrix solution* whose columns are solutions to Eq. (22) and  $\Phi(0)$  is the

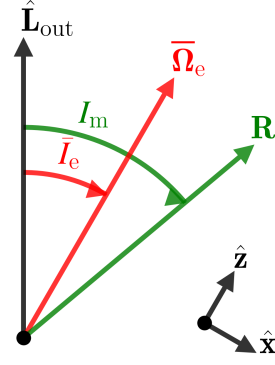


**Figure 16.** Definition of angles for numerical study of the monodromy matrix rotation axis.  $\mathbf{R}$  is the eigenvector of the monodromy matrix  $\tilde{\mathbf{M}}$  with eigenvalue 1.

identity.  $\mathbf{R}$  is then the eigenvector that has eigenvalue 1. Note that if  $\mathbf{v}$  is an eigenvector, so too is  $-\mathbf{v}$ ; we choose convention that  $\mathbf{R}$  points in the same direction as  $\bar{\Omega}_e$ , i.e.  $\Delta I_m \equiv |I_m - \bar{I}_e| < 90^\circ$ .

The orientation of  $\mathbf{R}$  is related to the  $|\Delta\bar{\theta}_e|$  predicted by Eq. (67): if  $\mathbf{R}$  and  $\bar{\Omega}_e$  are misaligned by angle  $\Delta I_m$ , then  $\bar{\theta}_e$  varies by up to  $2\Delta I_m$ . Thus, we can infer  $\Delta I_m$  in the vicinity of each  $\bar{\Omega}_e = N\Omega_{\text{LK}}$  resonance from Eq. (67). Finally, if the resonances are well spaced, the total  $\Delta I_m$  is well approximated by the sum of the contribution from each  $N$  harmonic, so

$$\Delta I_m \sim \sum_{N=1}^{\infty} \left| \frac{\sin \Delta I_{eN} \Omega_{eN}}{\bar{\Omega}_e - N\Omega_{\text{LK}}} \right|. \quad (\text{A14})$$

Fig. 17 shows that this calculation predicts the numeric  $\Delta I_m$  rather well except for the exact shape near  $I = 90^\circ$ . This tentatively supports our assertion that the primary deviation of  $\mathbf{R}$  from  $\bar{\Omega}_e$  comes at resonances  $\bar{\Omega}_e \approx N\Omega_{\text{LK}}$  whose effects are captured by Eq. (67).

This result suggests that our approximation in Section A.2 where the effect of nutation of  $\Omega_e$  is small except near resonance is largely accurate. We can qualitatively understand this if we assume that  $e^{\Phi'} \approx e^\Phi$  in Eq. (A10) (requiring small  $\bar{\mathbf{B}}$ , which we will verify retroactively, and being far from resonance), which gives

$$\bar{\mathbf{B}} \approx [e^{-\Phi}, \bar{\mathbf{A}}] e^\Phi. \quad (\text{A15})$$

Next, recall that  $\Phi$  is the integral of  $-\tilde{\mathbf{A}}$ , and so the magnitude of  $\bar{\mathbf{B}}$  [ $\bar{\mathbf{B}}$  primarily affects  $\tilde{\mathbf{M}}$  via its average, see Eq. (A11)] depends on the average misalignment between the vectors  $\Omega_e$  and  $\int' \Omega_e dt \approx \bar{\Omega}_e$ . There are a few possible regimes to consider: (i) if  $\mathcal{A} \gg 1$ , then LK oscillations are frozen, and  $\Omega_e$  does not nutate; (ii) if  $\mathcal{A} \ll 1$ , then  $\hat{\Omega}_e \approx \hat{\mathbf{L}}_{\text{tot}}$  for almost all of  $T_{\text{LK}}$ ; and (iii) if  $\mathcal{A} \approx 1$ , then  $j(e_{\text{max}})$  cannot be too small [Eq. (18)], and so  $d\bar{\Omega}_e/dt$  and  $\Omega_{\text{SL}}$  cannot vary too much within an LK cycle and the nutation of  $\Omega_e$  is limited. This implies



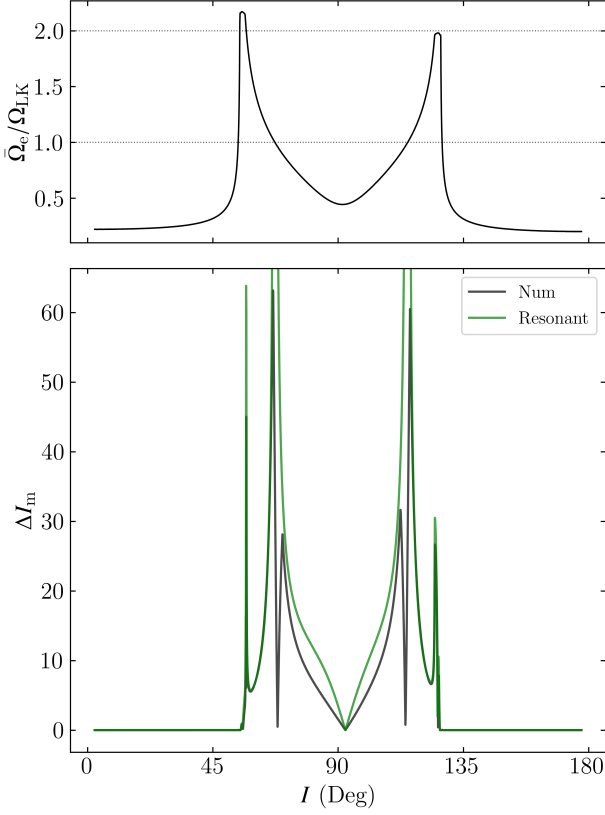


**Figure 17.** Comparison of the orientation  $\mathbf{R}$  obtained from numerical simulations with the analytic resonance formula given by Eq. (67) as a function of initial inclination, in the absence of GW dissipation. The top panel shows the ratio  $\Omega_e/\Omega_{LK}$  is shown as the solid black line, while the horizontal dashed lines denote  $\bar{\Omega}_e = \Omega_{LK}$  and  $\bar{\Omega}_e = 2\Omega_{LK}$ . The bottom panel shows the misalignment angle between  $\mathbf{R}$  and  $\bar{\Omega}_e$  as the black line. Separately, we can infer from Eq. (67) the effect of the  $N$ th harmonic on the misalignment between  $\bar{\Omega}_e$  and  $\mathbf{R}$ , given by Eq. (A14). We see that the scaling of the misalignment angle near resonance is generally well captured by our analytic formula, but the numerically computed misalignment angle is smaller than predicted near  $I = 90^\circ$ . Furthermore, the numeric misalignment angle crosses 0 within the  $N = 1$  resonance, which is not predicted by our simple theory.

that  $\tilde{\mathbf{B}}$  is likely small when far from resonance, justifying our prior claim. While this analysis is not rigorous, it gives a qualitative interpretation to the success of the approximation where nutation of  $\Omega_e$  is neglected except near resonances.

Finally, we take note of one difference between the resonance models in Section 5 and Appendix A.2. If only one harmonic exists, e.g.  $\Omega_{eN} = 0$  for  $N \geq 2$ , then Eq. (67) predicts that there should only be one resonance, at  $\bar{\Omega}_e = \Omega_{LK}$ , while Eq. (A11) suggests there should still be multiple resonances when  $\bar{\Omega}_e = N\Omega_{LK}$ . In the problem studied in this paper, this distinction is unimportant since  $\bar{\Omega}_e$  does not exceed a few  $\Omega_{LK}$ , and the first few harmonics  $\Omega_{eN}$  are quite

similar (the characteristic scale over which the  $\Omega_{eN}$  change is  $1/j(e_{\max}) \gg 1$ ), so the particular  $\Omega_{eN}$  responsible for a resonance makes little quantitative difference. **NB: Numerical experiments of a toy model suggest the latter picture is correct, but I am not sure I want to write this up.**